# The oxidation behavior and reaction thermodynamics and kinetics of the Mg-X (X = Ca/Gd/Y) binary alloys

Jiajia Wu [a,c], Yuan Yuan [a,c,*], Tao Chen [d], Aitao Tang [a], Liang Wu [a], Dajian Li [b], Martin Steinbrück [b], Fusheng Pan [a,c,*]

[a] National Engineering Research Center for Magnesium Alloys, College of Materials Science and Engineering, Chongqing University, Chongqing 400044, China
[b] Karlsruhe Institute of Technology, Institute for Applied Materials – Applied Materials Physics (IAM-AWP), Karlsruhe 76131, Germany
[c] International Joint Laboratory for Light Alloys (Ministry of Education), Chongqing University, Chongqing 400044, China
[d] Lanxi Magnesium Materials Research Institute, Lanxi 321100, China

ARTICLE INFO

*Keywords:*
Magnesium alloys
Oxidation
High temperature
Reactive elements

ABSTRACT

Oxidation behavior of the Mg-X (X Ca/Gd/Y) alloys at 500 ℃ was studied and had been clarified using thermodynamics and kinetics. The improved high-temperature oxidation resistance by reactive elements was attributed to the formation of compact reactive-element-rich oxide film. The oxides formation priority is determined by the critical concentration of reactive elements based on thermodynamics. A four-layered structure film was formed on Mg-Ca alloys, which was proposed to be caused by alternating enrichment of Ca and Mg atoms at metal/oxide interface. Hydrides was formed in the matrix during oxidation process, resulting from the decomposition of $H_2O$ and continues inward diffusion of H.

## 1. Introduction

Magnesium (Mg) alloys have the advantages of low density (2/3 of Al density), environmental friendliness, good thermal and electrical conductivity, etc., and attract increasing attentions in the fields of automobiles, aerospace and consumer electronics [1–5]. However, compared with many other metals, Mg alloys are oxidized quickly during processing under high-temperature environment (such as casting, welding, forging and heat treatment) and in the medium temperature service [6–9]. In order to prevent the catastrophic oxidation and combustion during the manufacturing process of Mg alloys, the research on the oxidation-resistance of Mg alloys at high temperature is of great importance to extend their engineering application.

When exposed to the atmosphere at high temperature (higher than 450 ℃), Mg tends to form a loose-structure MgO film on the surface, which is unable to effectively isolate oxygen from the Mg matrix and avoid the catastrophic oxidation owing to the low Pilling-Bedworth ratio ($R_{PB}$) of MgO (0.81) [6,10–13]. Alloying and surface modification are two main methods to improve the oxidation resistance of Mg alloys at high temperature [11,14–16]. The alloying method is simple and fundamental method to tailor the alloys' properties [8,17–32] and widely adopted to improve the oxidation resistance of Mg alloys at high temperature.

It is accepted that reactive elements, such as alkaline earth elements (Ca, Be) and rare earth (RE) elements (Nd, Gd, Ce, La, etc.), can improve the oxidation resistance of Mg alloys at high temperature [6,12,13,16,27,33–41]. Among them, the effects of alkaline earth elements Ca and Be in Al-containing Mg alloys have been widely studied [8,16,24–27,34–37]. Dong [27] found that the alloys of AZ31 + 0.3 wt% Ca and AZ31 + 0.3 wt% CaO could be cast in ambient air without using environmentally hazardous $SF_6$ gas, by forming a thin CaO-rich barrier layer on the surface during casting. Tan [16,36,37] reported that the oxidation resistance of AZ91 alloy could be effectively improved by micro-alloying with 60 ppm Be. It was claimed that the Be element participated in the formation of solid solution (Mg, Be)O, which provided sufficient strength to withstand the internal stress and Mg vaporization, therefore delayed the oxide film cracking and debonding from the substrate. In addition, RE elements are also believed to improve the oxidation resistance at high temperature, especially for Mg alloy systems without Al. Adyin [42] showed that dilute Mg-Nd alloys (up to 0.5 wt% Nd) had better oxidation and ignition resistance compared with pure Mg, which was attributed to the formation of a composite

* Corresponding authors at: National Engineering Research Center for Magnesium Alloys, College of Materials Science and Engineering, Chongqing University, Chongqing 400044, China.
*E-mail addresses:* yuanyuan17@cqu.edu.cn, yuan.yuan.er@gmail.com (Y. Yuan), fspan@cqu.edu.cn (F. Pan).

MgO-$Nd_2O_3$ film. Wang [40] proved that Mg-10Gd-3Y alloy obeyed the protective oxidation over the temperature range of 450–600 ℃ in pure $O_2$ up to 90 min. A continuous $Gd_2O_3/Y_2O_3$ oxide was formed on the surface, which could reduce the inward diffusion of oxygen.

Although the high-temperature oxidation performance of Mg alloys is attracting increasing attention, the related thermodynamics, kinetics and mechanism are still not clear. Most researches focus on the influence of a single reactive element, while differences between reactive elements in terms of oxidizing effects are not reported. In this work, the alkaline earth element Ca and the rare earth elements Gd and Y, with large differences in atomic number, were selected to systematically study the influence of reactive element types and contents on the oxidation behavior, and a general oxidation mechanism was proposed.

## 2. Experimental methods

### 2.1. Alloy preparation

In this work, commercial pure Mg and master alloys of Mg-30 wt% Ca, Mg-30 wt% Gd and Mg-30 wt% Y were selected as raw materials for manufacture of the as-cast alloys. The raw materials were heated to 740 ℃ in a resistance furnace. After complete melting, the melt was thoroughly stirred and then taken out to cooled down to room temperature. The entire melting process was carried out under the protection of a mixed gas, 99 vol% $CO_2$-1 vol% $SF_6$. The chemical compositions of the synthesized alloys are shown in Table 1, which were detected by X-ray fluorescence spectroscopy (XRF). The obtained ingots were cut into blocks. Then they were ground to 1200 grit SiC sandpaper and rinsed with alcohol for subsequent oxidation behavior test and structural characterization.

### 2.2. Oxidation tests

The high-temperature oxidation of specimens was conducted in a box furnace, and the ambient air was used as the oxidizing atmosphere to simulate the ordinary heat treatment environment of Mg alloys, which contains traces of water vapor and $CO_2$. The oxidation temperature was set at 500 ℃, which is the common temperature for the heat treatment process of Mg alloys. A semi in-situ method was used to conduct the oxidation weight gain test. During this test, the specimens were periodically taken out from the furnace and cooled down to room temperature for weight measurement, and then put back into the furnace for subsequent oxidation. Specimens were weighed using a precision analytical balance (METTLER MS10$^5$/A, accuracy 10$^{-5}$ g).

### 2.3. Microstructural characterization and thermodynamic calculation

The microstructures of the as-cast and oxidized alloys were characterized using scanning electron microscopy (FE-SEM, JEOL JSM-7800 F) equipped with energy dispersive spectroscopy (EDS), with 15 kV voltage and 12 mA current. The volume fraction of the second phase in the alloys was counted by Image-J software, and the statistical result was the average of the five images for each specimen. The phase identification of the as-cast and oxidized alloys was conducted by X-ray diffraction (XRD, Rigaku D/MAX-1200 and D/MAX-2500 PC), with Cu targets, 10–90° scanning range, 40 kV voltage, and 30 mA current. Auger electron spectrometry (AES, PHI 710e/680 Hybrid Auger Nanoprobe) was used to detect the depth distribution of elements in the oxide film.

Binary phase diagrams of Mg-Ca, Mg-Gd, Mg-Y systems were calculated using Thermal-Calc software equipped with the TCMG5 database. The standard Gibbs free energy changes for oxidation reactions were calculated using Factsage (version 7.0) software.

**Table 1**
Chemical compositions of the Mg-X (X  Ca/Gd/Y) binary alloys.

| Alloys | Ca (wt%/at%) | Gd (wt%/at%) | Y (wt%/at%) | Mg |
|---|---|---|---|---|
| C1 | 0.5/0.3 | / | / | Bal. |
| C2 | 2.4/1.5 | / | / | Bal. |
| G1 | / | 3.3/0.5 | / | Bal. |
| G2 | / | 4.7/0.8 | / | Bal. |
| G3 | / | 10.0/1.7 | / | Bal. |
| Y1 | / | / | 3.7/1.0 | Bal. |
| Y2 | / | / | 10.0/3.0 | Bal. |
| Y3 | / | / | 14.2/4.3 | Bal. |

## 3. Results

### 3.1. The microstructure of the as-cast alloys

Fig. 1 shows the backscattered electron (BSE) images, XRD patterns of the as-cast Mg-Ca binary alloys, and the phase diagram of the Mg-Ca system. As shown in Fig. 1(a1), there is no obvious second phase in the C1 alloy, where Ca is mainly dissolved in α-Mg. For the C2 alloy, the network-structure second phase is formed along the grain boundaries, which is identified as the $Mg_2Ca$ phase according to the XRD results in Fig. 1(b). Fig. 1(c) shows the Mg-rich corner of the phase diagram of the Mg-Ca binary system. During the solidification process of the C2 alloy, when the temperature drops to the eutectic temperature of 515 ℃, the alloy undergoes the eutectic reaction: Liquid→α-Mg+$Mg_2Ca$, thus forming a eutectic structure distributed along the grain boundaries as shown in Fig. 1(a2).

Fig. 2 shows the BSE images, XRD patterns, and the phase diagram of the Mg-Gd binary system. As shown in Fig. 2(a1)-(a3), the distinctive characteristic on microstructure of the Mg-Gd alloys is that the grain boundaries are presented as gray-white blurred state, which is caused by the segregation of Gd atoms along the grain boundaries. The segregation of alloying elements along grain boundaries is commonly observed in the as-cast Mg alloys [13,43]. Its formation is caused by the rapid cooling speed during the solidification process, during which the solute atoms cannot fully diffuse to form the second phase but are segregated at grain boundaries. For the G3 alloy, with higher Gd content, the second phase is formed from the segregation area. It can be seen from the XRD results in Fig. 2(b) that the second phase is the $Mg_5Gd$ phase. According to the phase diagram of the Mg-Gd system in Fig. 2(c), when the Gd content is less than 20.1 wt%, the alloy does not undergo the eutectic reaction during the solidification process. Therefore, none of the Mg-Gd alloys in this work form eutectic structure.

As shown in Fig. 3(a1)-(a3), the microstructure of the Mg-Y alloys is similar to that of the Mg-Gd alloys, which is composed of Y element segregation area along the grain boundaries. For the Y2 and Y3 alloys with higher Y content, a large amount of second phase is precipitated from the segregation area, and the second phase content increases with the increment of Y content. According to the XRD results in Fig. 3(b), $Mg_{24}Y_5$ phase is present in the Y2 and Y3 alloys, and its content in the Y3 alloy is greater than that of the Y2 alloy, which is consistent with the demonstration in the Fig. 3(a1)-(a3). As shown in Fig. 3(c), when the Y content exceeds 12.1 wt%, the alloy will undergo the eutectic reaction at 567 ℃ during solidification process: Liquid→α-Mg+$Mg_{24}Y_5$. Therefore, the Y3 alloy (14.2 wt% Y) forms a network eutectic structure along the grain boundaries. It is worth noting that the Y2 alloy also forms eutectic structure, as shown in Fig. 3(a2), although its Y content (10.0 wt%) is less than 12.1 wt%. This can be attributed to the non-equilibrium solidification caused by the actual fast cooling rate.

### 3.2. Oxidation kinetics

Fig. 4(a) and (b) displays the variation of oxidation weight gain with time for pure Mg and Mg-X (X = Ca/Gd/Y) binary alloys at 500 ℃, in which pure Mg is set as the reference. As shown in Fig. 4(a), the weight gain of pure Mg is as high as 5.44 mg·cm$^{-2}$ after the oxidation for 22 h, which is significantly greater than that of the binary alloys. The weight gain measurement of pure Mg does not continue after 22 h due to the

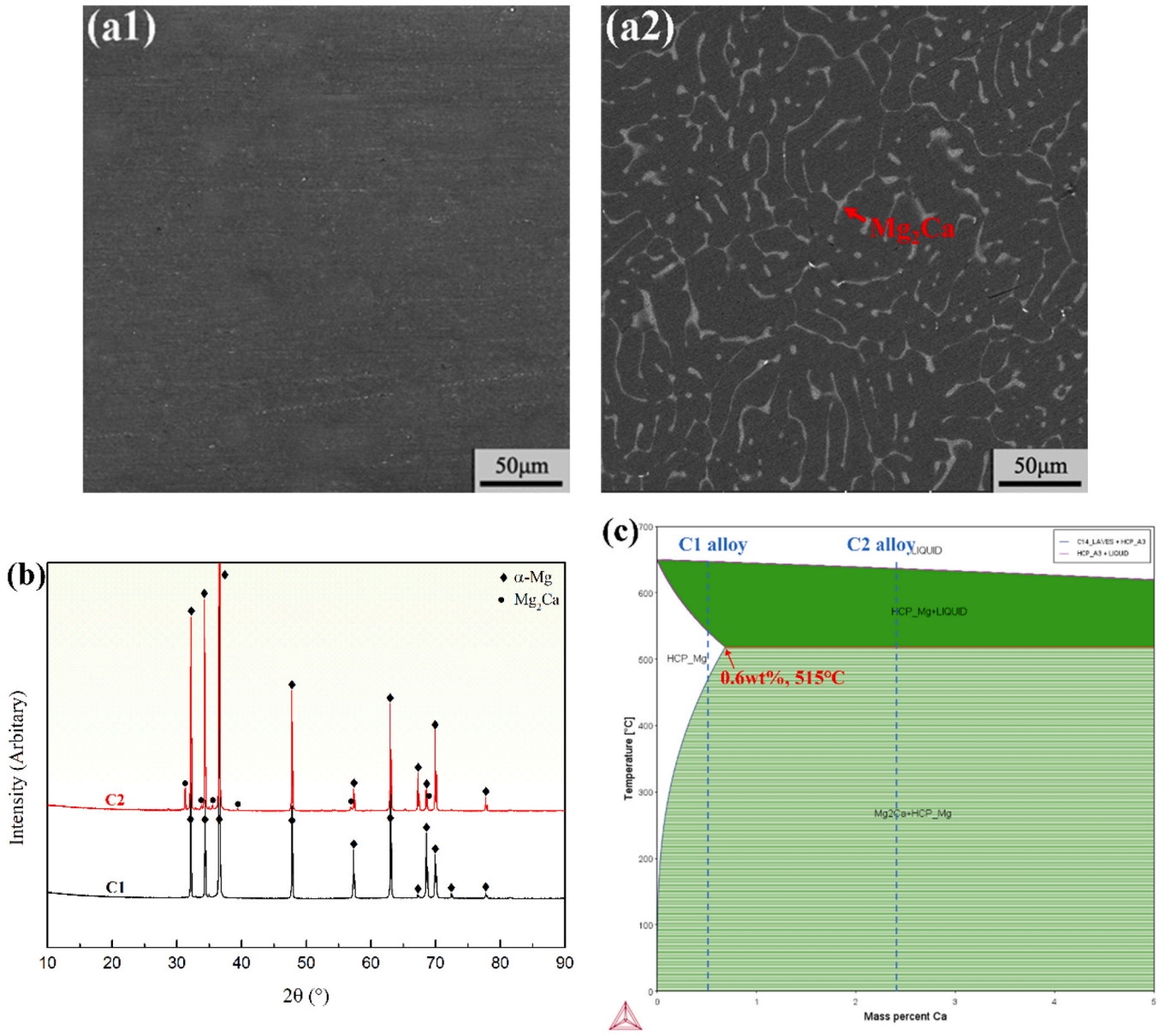


**Fig. 1.** Backscattered electron images (BSE) of the as-cast Mg-Ca binary alloys: (a1) C1, (a2) C2, (b) the XRD patterns and (c) the phase diagram of Mg-Ca system calculated using Thermo-Calc software.

shedding of a large amount of MgO powder in subsequent oxidation, leading to weighing errors. The above results indicate that the addition of reactive elements can greatly improve the high-temperature oxidation resistance of Mg. Pure Mg exhibits acceleration in weight gain at the beginning of oxidation, and its variation of weight gain can be fitted to the power law using the following equation [6,37,44]:

$$\Delta m = At^n + B(n > 1) \quad (1)$$

where $\Delta m$ is the weight gain per unit area (mg·cm $^{2}$), A and B are the fitting constants, $n$ is the exponent, and $t$ represents the oxidation time in hours. The fitted curve is shown as the solid line in Fig. 4(a), and the kinetic parameters are shown in Table 2. Fig. 4(b) shows regional enlargement of Fig. 4(a), which clearly demonstrates the variation of weight gain for the Mg-X (X = Ca/Gd/Y) binary alloys. In order to determine the oxidation kinetics of these binary alloys, the square of weight gain is calculated, as shown in Fig. 4(c). It can be seen that the square of weight gain of all binary alloys is approximately linear with time, which means that the oxidation of these alloys follows parabolic oxidation kinetics, and its weight gain can be fitted to the parabolic law using the following equation [6,37,39,44]:

$$\Delta m = (k_p \cdot t)^{\frac{1}{2}} \quad (2)$$

where $k_p$ is the parabolic rate constant (mg$^2$·cm $^{4}$·h $^{1}$). The fitted curves are displayed in solid line in Fig. 4(b), and the fitting parameters are shown in Table 2.

Oxidation kinetics can be used to evaluate the oxidation resistance of alloys. According to the above results, pure Mg obeys power law oxidation kinetics, which is a non-protective oxidation and the oxidation rate increases with time. In contrast, parabolic oxidation kinetics correspond to the protective oxidation, and the compact oxide film is believed to be formed on the surface of the alloy. According to Wagner's oxidation theory, the oxidation process following the parabolic kinetics is controlled by the diffusion of ions across the oxide film. Therefore, the binary alloys in this work have superior oxidation resistance at 500 ℃. In addition, it can be seen from Table 2 that the parabolic rate constant ($k_p$) also increases with the increased content of reactive element. In

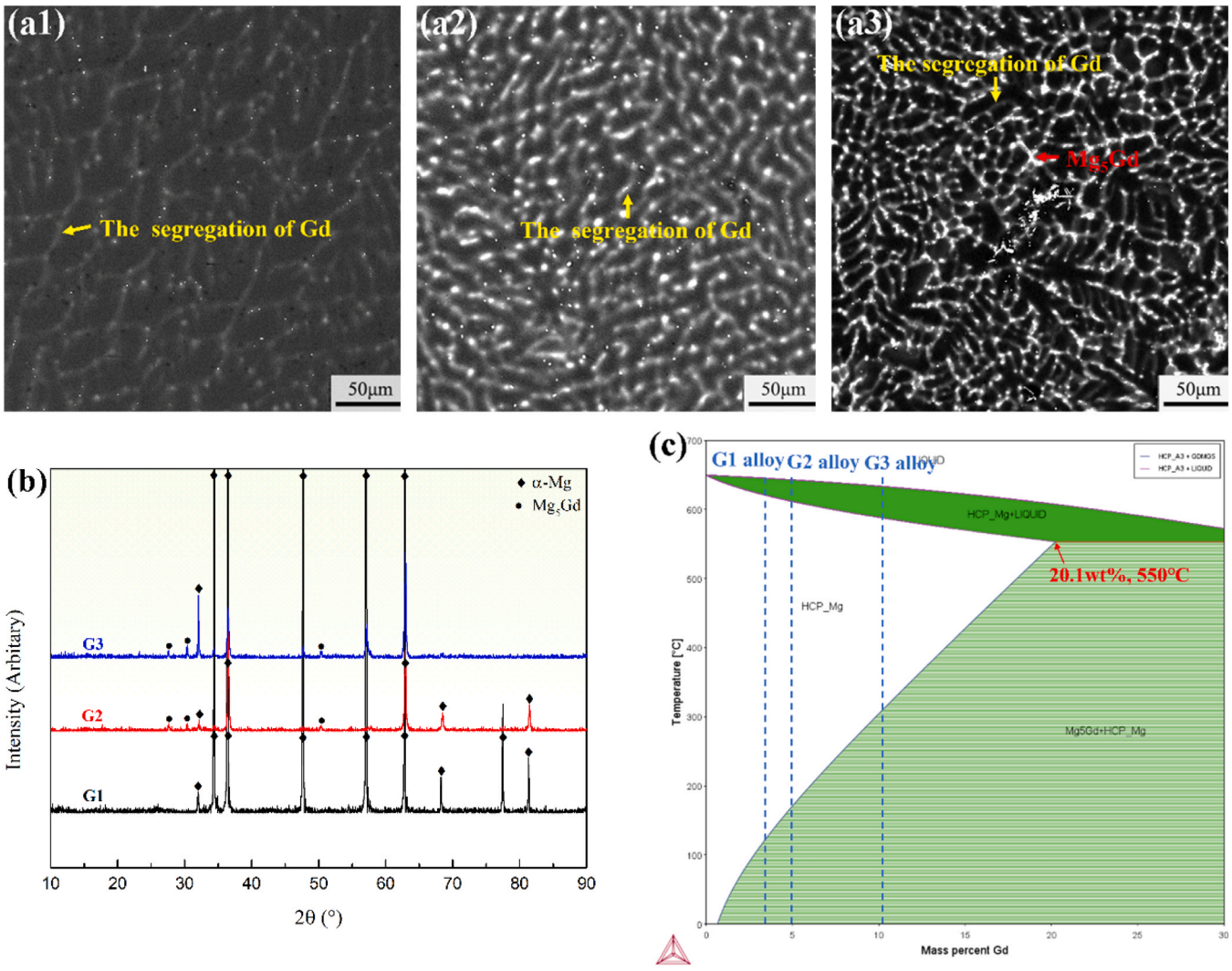


**Fig. 2.** Backscattered electron images (BSE) of the as-cast Mg-Gd binary alloys: (a1) G1, (a2) G2, (a3) G3, (b) the XRD patterns and (c) the phase diagram of Mg-Gd system calculated using Thermo-Calc software.

addition, it can be seen from Table 2 that the $k_p$ is related to the type of alloying elements. The $k_p$ of the Mg-Ca alloys is significantly smaller than that of the Mg-Gd and Mg-Y alloys, which indicates that the oxidation rate of the Mg-Ca alloys is smaller than that of the Mg-Gd and Mg-Y alloys.

### 3.3. Macrographs after oxidation

Fig. 5 shows the macrographs of pure Mg and the Mg-X (X = Ca/Gd/Y) binary alloys after oxidation at 500 ℃ for 100 h. Pure Mg is severely oxidized, and the surface is completely covered with loose white oxide powder, which falls off during sample transportation. However, the surfaces of all binary alloys after oxidation are covered with flat and compact oxide film, indicating that these alloys exhibit excellent high-temperature oxidation resistance.

### 3.4. Oxide films analysis

The XRD patterns of the oxidized binary alloys are shown in Fig. 6, where the strong α-Mg peaks come from the Mg matrix, indicating that the oxide films of these alloys are thin. It can be seen from Fig. 6(a) that the oxide films of Mg-Ca alloys are mainly composed of CaO and $CaCO_3$, of which CaO is the main component. $CaCO_3$ is formed by the reaction of CaO with $CO_2$ in the air [11,15]. For the Mg-Gd and Mg-Y alloys, as shown in Fig. 6(b) (c), only $Gd_2O_3$ or $Y_2O_3$ is detected from the oxide film, which means that the oxide films of the Mg-Gd and Mg-Y alloys are mainly composed of $Gd_2O_3$ and $Y_2O_3$. In addition, with the increment of Gd/Y content, the $Gd_2O_3/Y_2O_3$ peaks intensify, indicating that the amount of $Gd_2O_3/Y_2O_3$ also increases. In summary, the oxide films formed on the Mg-Ca, Mg-Gd and Mg-Y binary alloys at 500 ℃ are mainly composed of their respective reactive element oxides or carbonates.

Fig. 7 displays the microstructure of the oxide films formed on the binary alloys after the oxidation at 500 ℃ for 100 h. All oxide films are flat and compact, which is consistent with their parabolic oxidation kinetics. For the Mg-Ca alloys, the oxide grain size of the C1 alloy is about 500 nm, while it is extremely small for the C2 alloy. Therefore, the oxide grain size decreases significantly with the increment of Ca content. Aydin [45] and Yu [43] also found the similar phenomenon in the Mg-Y and Mg-Nd alloys. For the Mg-Gd alloys, their oxide films exhibit the alternative distribution of light and dark morphology, especially for the G1 alloy (with less Gd content). This morphology is speculated to be caused by heterogeneity of the oxides, which induces different secondary electron emission quantities and different brightness regions. Therefore, the elements distribution of oxide film formed on G1 and G3 alloys is characterized by EDS, as shown in Fig. 8. It can be found that the bright region is enriched with Gd, and the dark region is enriched with Mg. Combined with XRD results, it can be inferred that the bright

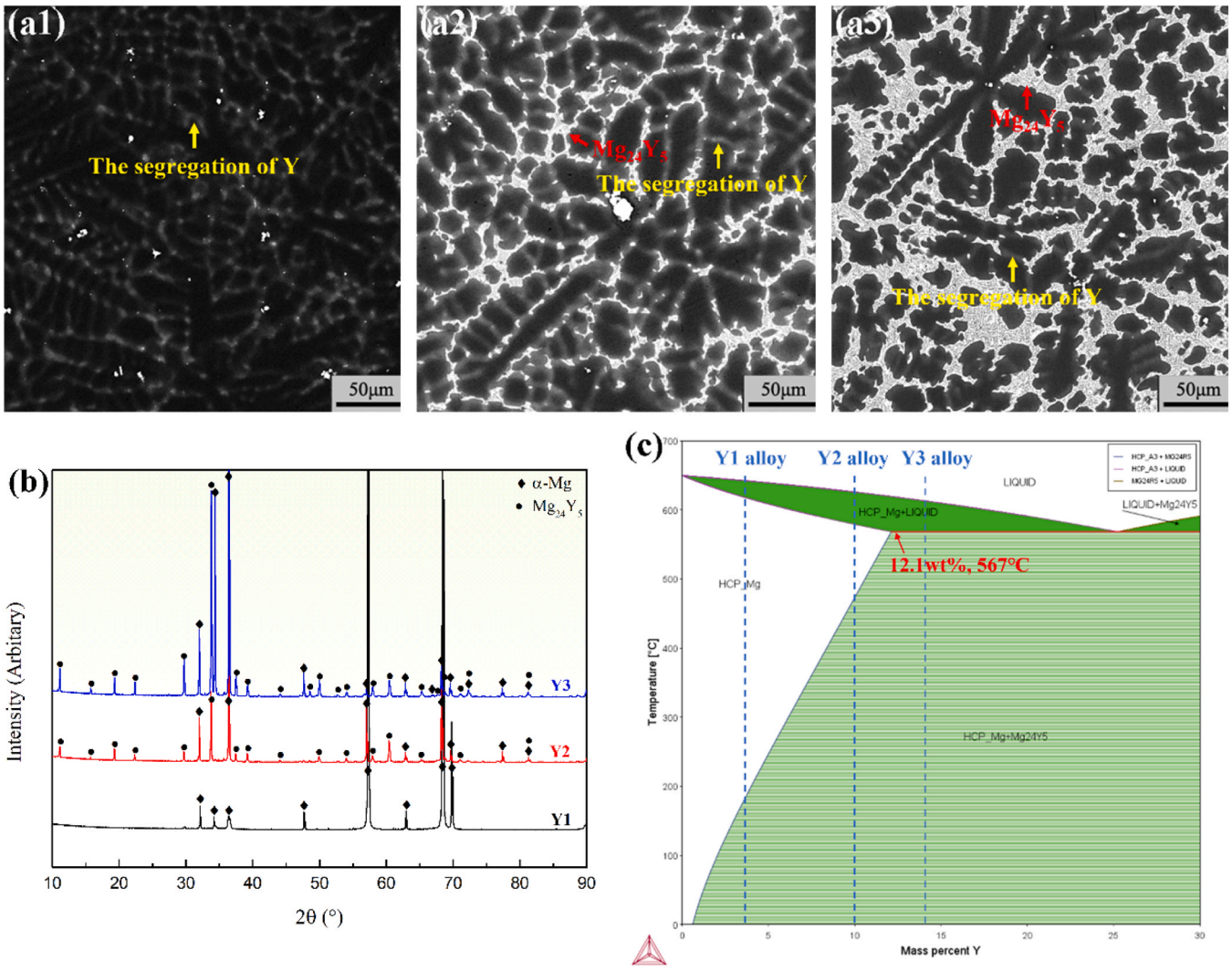


**Fig. 3.** Backscattered electron images (BSE) of the as-cast Mg-Y binary alloys: (a1) Y1, (a2) Y2, (a3) Y3, (b) the XRD patterns and (c) the phase diagram of Mg-Y system calculated using Thermo-Calc software.

region corresponds to $Gd_2O_3$, and the dark region corresponds to MgO. As for Mg-Y binary alloys, compact and uniform oxide films are formed on the surface, which is almost composed of $Y_2O_3$.

In order to analyze the formation process of the oxide film, the cross section of the alloys after oxidation is characterized. Fig. 9 shows the cross-sectional BSE images and the corresponding EDS element maps. As shown in Fig. 9(a) (b), the enrichment of Ca and O take place on the surface of Mg-Ca binary alloys, indicating that the oxide films are mainly composed of Ca-rich compounds, which is consistent with the XRD results in Fig. 6. Since the formation of the reactive-element-rich oxide film on the surface depends on the replenishment of the reactive element from the sublayer, the metal matrix is also of interest. Since the deep matrix is partially exhibited in Fig. 9, BSE image of the deep matrix is shown in Fig. 10, displaying the structure of this area more clearly. As shown in Fig. 9(a) and Fig. 10(a), there is no second phase in the matrix of the C1 alloy, where the Ca element is completely soluble in α-Mg. For the C2 alloy, as shown in Fig. 9(b) and Fig. 10(b), there is a large number of $Mg_2Ca$ phase in the deep matrix. Different from the eutectic structure existed in the as-cast alloy, $Mg_2Ca$ is transformed into island shape after oxidation at 500 ℃. In addition, as shown in Fig. 9(b), a second phase depleted zone (zone_1) is formed at the sublayer of the oxide film in the C2 alloy, with the thickness of about 70 μm. The formation of the depleted zone indicates the occurring of the dissolution of the $Mg_2Ca$ phase and the outward diffusion of Ca atoms in the sublayer. Since the formation of the Ca-rich oxide film on the surface constantly consumes Ca atoms, the Ca atoms in sublayer continue to diffuse towards the surface of the alloy, resulting in a gradual decrease of the concentration of Ca in the α-Mg in sublayer. According to the phase diagram in Fig. 1 (c), the solid solubility of Ca in α-Mg at 500 ℃ is 0.61 wt%. When the concentration of Ca in the sublayer decreases to this value, the $Mg_2Ca$ phase will dissolve to supplement the consumption of outward diffusion. When the $Mg_2Ca$ phase near the oxide film is completely dissolved, the deeper $Mg_2Ca$ phase will be further dissolved with the progressing of oxidation, so that the second phase depleted zone continues to advance deeper. For the Mg-Gd alloys, as shown in Fig. 9(c) (d) (e), a large number of Gd elements are enriched at the oxide films, which indicates that the oxide films are mainly composed of $Gd_2O_3$, and it is consistent with the XRD results in Fig. 7. It is worth noting that the second phase depeltion zone (zone_1) also exists in the sublayer of Mg-Gd alloys, and the thicknesses of the G1, G2 and G3 alloys are 90 μm, 130 μm and 130 μm, respectively. Fine white second phase particles are dispersed in the deep matrix (zone_2) of Mg-Gd alloys. Due to the small size of the second phase in Fig. 9, the elemental distribution measured by EDS may be skewed. In order to more accurately reflect the elemental distribution of these second phases, the area in G1 alloy with larger second phases is selected for further EDS analysis, as shown in Fig. 10(i). It can be seen that these second phases are cuboid-shape and almost only Gd element is detected, which indicates that the second phase cannot be $Mg_5Gd$ phase.

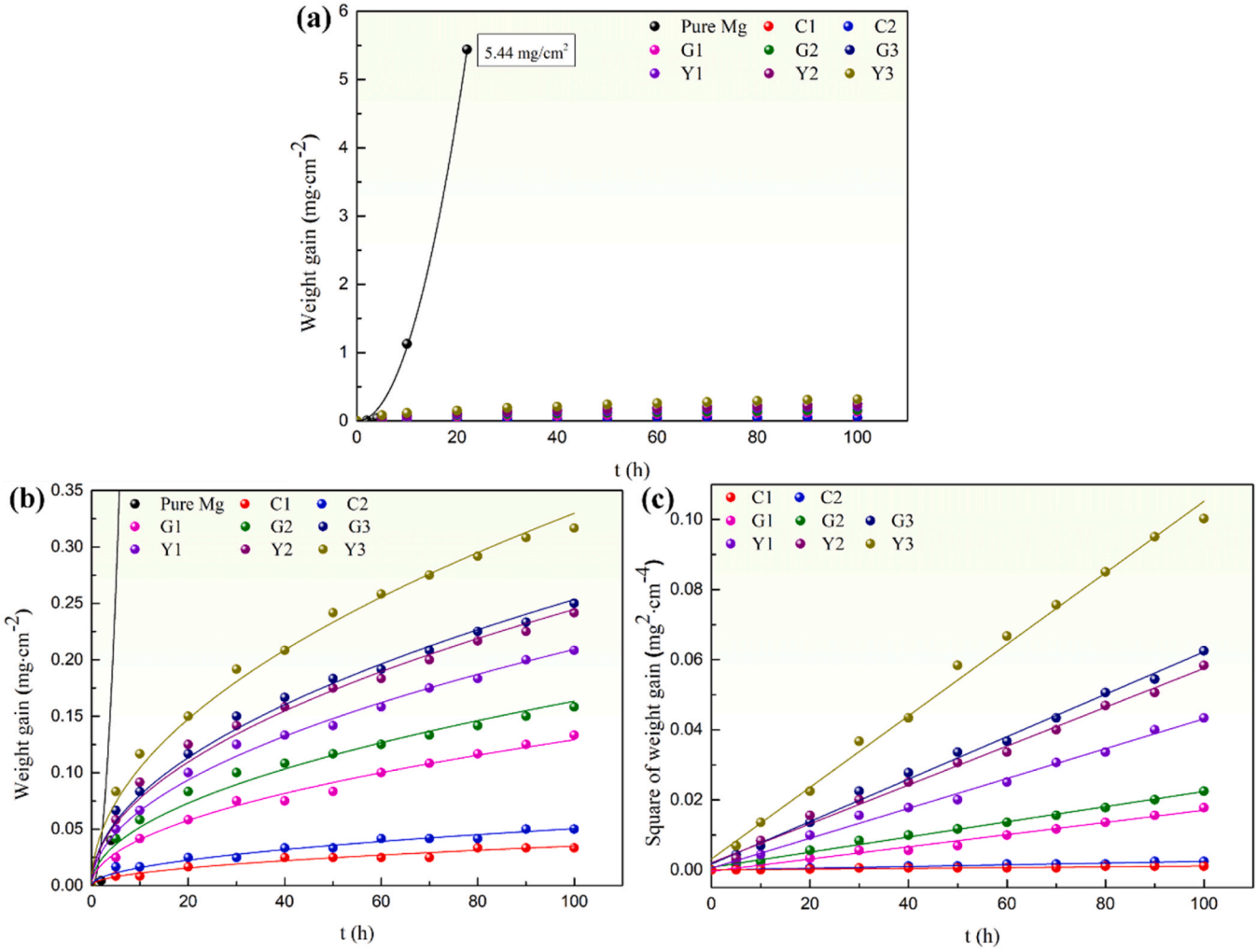


**Fig. 4.** Oxidation kinetic curves of pure Mg and the Mg-X (X Ca/Gd/Y) binary alloys at 500 ℃ for 100 h: (a) weight gain curves, (b) the regional enlargement of (a), (c) square of weight gain curves.

**Table 2**
Oxidation kinetic parameters of pure Mg and the binary alloys (kp: $mg^2 \cdot cm^{-4} \cdot h^{-1}$).

| Alloys | Oxidation periods | Oxidation kinetics | Parameters | $R^2$ |
|---|---|---|---|---|
| Pure Mg | $0 < t < 22$ h | Power | $n = 2.06$, $A = 9.43 \times 10^{3}$ | 0.99 |
| C1 | $0 < t < 100$ h | Parabolic | $k_p = 1.23 \times 10^{5}$ | 0.90 |
| C2 | $0 < t < 100$ h | Parabolic | $k_p = 2.55 \times 10^{5}$ | 0.95 |
| G1 | $0 < t < 100$ h | Parabolic | $k_p = 1.67 \times 10^{4}$ | 0.99 |
| G2 | $0 < t < 100$ h | Parabolic | $k_p = 2.67 \times 10^{4}$ | 0.97 |
| G3 | $0 < t < 100$ h | Parabolic | $k_p = 6.42 \times 10^{4}$ | 0.99 |
| Y1 | $0 < t < 100$ h | Parabolic | $k_p = 4.38 \times 10^{4}$ | 0.99 |
| Y2 | $0 < t < 100$ h | Parabolic | $k_p = 5.95 \times 10^{4}$ | 0.99 |
| Y3 | $0 < t < 100$ h | Parabolic | $k_p = 1.02 \times 10^{3}$ | 0.99 |

To identify the cuboid phase, XRD analysis is performed on the matrix of the G3 alloy, as shown in Fig. 11(a). XRD result shows that the cuboid phase is the $GdH_2$ phase. The $GdH_2$ phase is formed by the reaction of Gd element with $H_2$ at high temperatures, and other scholars [46–50] have also found similar rare earth hydrides in rare-earth-containing Mg alloys after high-temperature treatment. For Mg-Y alloys, as shown in Fig. 9(f) (g) (h), Y element are enriched at the oxide films, indicating the oxide films composing of $Y_2O_3$, which is consistent with the XRD results in Fig. 7. The second phase depeltion zone (zone_1) is also found in the Mg-Y alloys, and the thickness of the Y1, Y2 and Y3 alloys is 90 μm, 60 μm and 25 μm, respectively. It can be found that the thickness of the depleted zone decreases with the increased content of Y. This may be due to the large difference in the Y content in the Y1, Y2 and Y3 alloys, so that the alloy with more Y content can provide higher amount of Y per unit volume metal, resulting in a narrower depeltion zone. In addition, it is worth noting that there is significant difference in the second phase in the matrix of these three alloys. The Y1 alloy mainly contains the cuboid phase, which is similar to that found in the Mg-Gd alloys. EDS results imply that the cuboid phase almost only contains Y element and does not contain Mg element, so it cannot be $Mg_{24}Y_5$ phase. In order to identify this phase, XRD analysis is performed on the matrix of the Y1 alloy, as shown in Fig. 11(b), and the results show that the cuboid phase is $YH_2$ phase. Different from the Y1 alloy, the second phase regions in the Y2 and Y3 alloys exhibit a layered structure, which constists of a single-phase layer of cuboid phase $YH_2$ (zone_2) and a duplex layer coexisting with $YH_2$ phase and $Mg_{24}Y_5$ phase in the deep matrix (zone_3). The volume fraction of the second phase in zone_3 of each alloy is counted using Image-J software, and the result is shown in Fig. 12. It can be seen that the phase in zone_3 is dominated by the $Mg_{24}Y_5$ phase, while the amount of $YH_2$ phase is relatively small. The eutectic structure of $Mg_{24}Y_5$ phase in the as-cast state of Y2 and Y3 alloys (Fig. 3) disappears after the oxidation treament, which is similar to the Mg-Ca alloys. The thicknesses of zone_2 in the Y2 and Y3 alloys are 150 μm and 65 μm, respectively. The size of $YH_2$ phase in zone_2 is

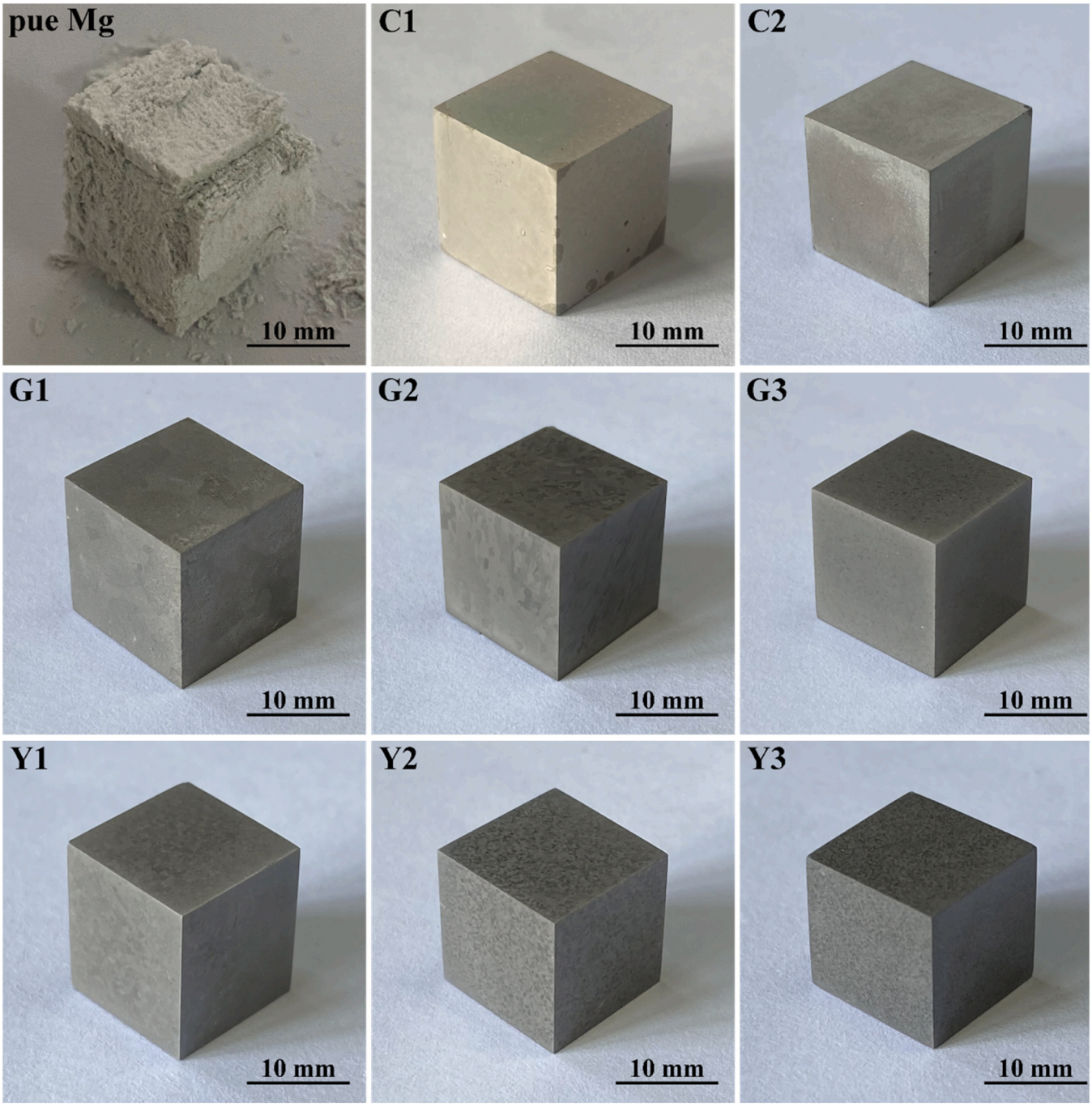


**Fig. 5.** Macrographs of pure Mg and the Mg-X (X Ca/Gd/Y) binary alloys after the oxidation at 500 ℃ for 100 h.

significantly smaller than that in zone_3, and the $YH_2$ phase is obviously precipitated along the grain boundaries.

The previous XRD and EDS analyses have clarified the main components of the oxide film. In order to quantify the distribution of elements in the depth of the oxide film, AES is performed and the results are shown in Fig. 13. As shown in Fig. 13(a) (b), the oxide films of the Mg-Ca alloys exhibit a four-layered structure, in which MgO and CaO are distributed alternately, indicating that the two oxides are alternately formed during the oxidation process. The oxide film of the C1 alloy from the outside to the inside can be divided into CaO-rich layer, MgO layer, CaO layer, CaO and MgO mixed layer, respectively. The oxide film of the C2 alloy from the outside to the inside can be divided into CaO-rich layer, CaO and MgO mixed layer, CaO layer, CaO and MgO mixed layer, respectively. It is worth noting that a small amount of C is detected on the outside of the C1 alloy. According to the previous XRD results, there is a small amount of $CaCO_3$ in the oxide film, so it is speculated that the C detected here comes from $CaCO_3$. $CaCO_3$ is formed by reacting CaO with $CO_2$ existed in air, which is thermodynamically feasible below 521 ℃ [15]. According to Fig. 13(a), the amount of $CaCO_3$ in the oxide film is quite small, so it can be considered that Ca mainly participates in the formation of CaO during the oxidation process. The relative content of CaO and MgO can be obtained by integrating the curves of Ca and Mg (MgO) in Fig. 13(a) (b), and the oxide proportion ($r_{(CaO/MgO)}$) is shown in Fig. 14. The $r_{(CaO/MgO)}$ values of the C1 and C2 alloys are 1.33 and 2.85, respectively, indicating that the proportion of CaO in the oxide film increased with the increment of Ca addition. As shown in Fig. 13(c) (d) (e), for the Mg-Gd alloys, the oxide films are composed of $Gd_2O_3$ and MgO, and MgO is mainly distributed in the outer layer. Fig. 14 shows the

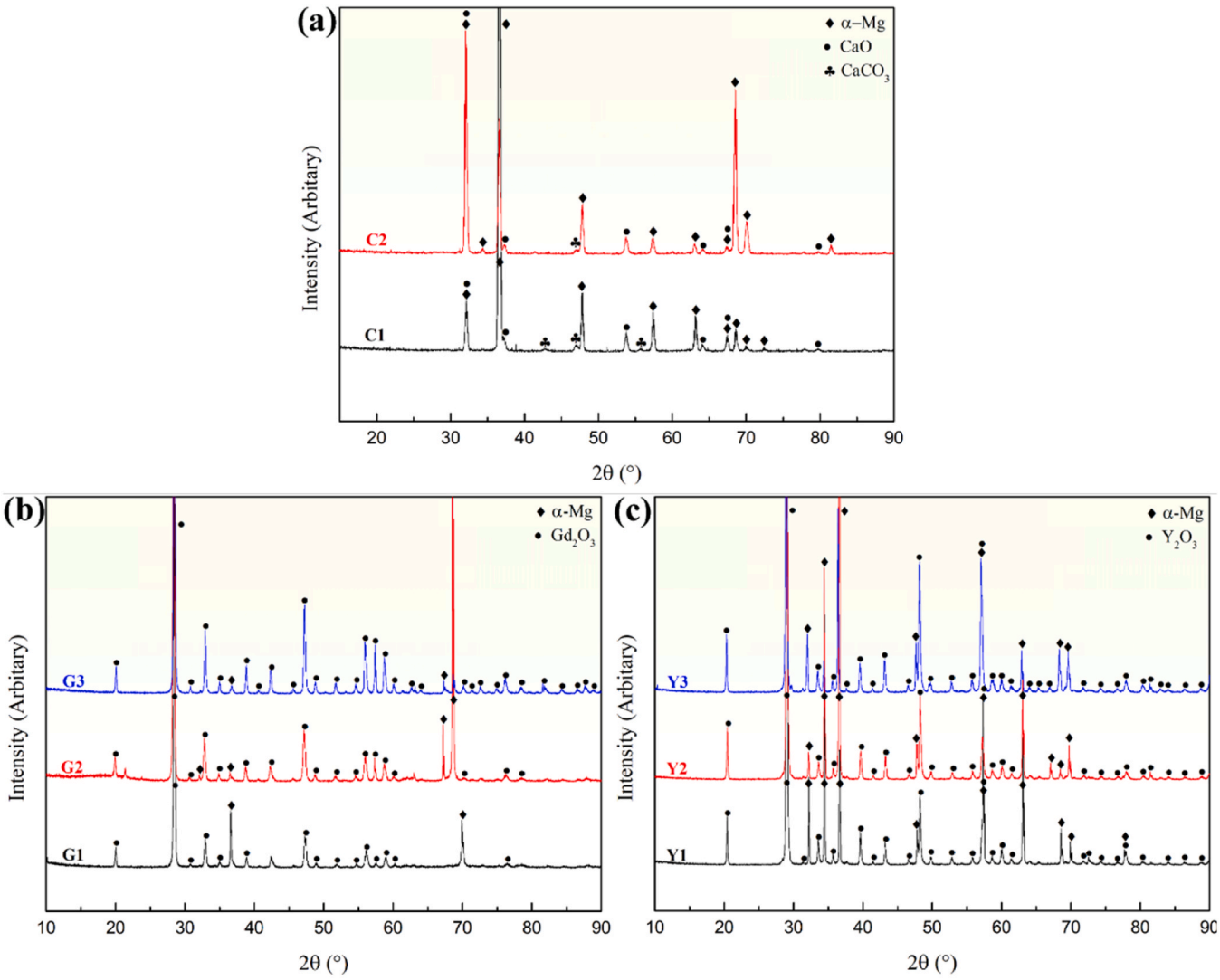


**Fig. 6.** XRD patterns of oxidized alloys: (a) Mg-Ca alloys, (b) Mg-Gd alloys, (c) Mg-Y alloys.

oxide proportion ($r_{(Gd2O3/MgO)}$), and the $r_{(Gd2O3/MgO)}$ values of the G1, G2 and G3 alloys are 1.56, 1.74 and 7.78, respectively. Like the Mg-Ca alloys, the proportion of $Gd_2O_3$ in the Mg-Gd alloys also increases with the increasing addition of Gd. As shown in Fig. 13(f)-(h), the oxide films of the Mg-Y alloys are completely composed of $Y_2O_3$.

## 4. Discussion

### 4.1. Protectiveness of oxide films

According to the weight gain curves in Fig. 4, the Mg-X (X = Ca/Gd/Y) binary alloys investigated in this work follow protective oxidation at 500 ℃, while pure Mg undergoes accelerated oxidation. As shown in Fig. 5 and Fig. 7, a large amount of loose MgO is formed on the surface of pure Mg, while compact and uniform oxide films are formed on the surface of these binary alloys. The compactness of the oxide film is an important factor to determine the oxidation resistance of alloys [1,2,14,16,23,37]. The loose oxide film formed on pure Mg cannot effectively isolate the metal from the contact with oxidizing atmosphere, so it fails in inhibiting the subsequent oxidation. However, the compact rare-earth-rich oxide films formed on the binary alloys can effectively isolate internal metals from oxygen and hinder oxidation. The compactness of an oxide film can be reflected by the Pilling-Bedworth ratio ($R_{PB}$) [11,22,24,41,51], which is expressed as the ratio of the volume of the generated oxide to the volume of metal consumed:

$$R_{PB} = \frac{M_{oxide}\ \ \rho_{metal}}{nM_{metal}\ \ \rho_{oxide}} \quad (2)$$

where $M$ is the mass of an atom or molecule. $n$ is the number of metal atoms in the oxide molecule. $\rho$ represents density.

If the $R_{PB}$ is less than 1, the oxide film cannot completely cover the metal matrix, and the loose structure provides insufficient protection for the matrix. If the $R_{PB}$ ranges from 1 to 2, the oxide film is compact and protective. If the $R_{PB}$ is larger than 2, cracking and peeling of the oxide film occur due to the enormous compressive stress within the film [24,51]. According to Eq. (2), the $R_{PB}$ of MgO/alloy, CaO/alloy, $Y_2O_3$/alloy and $Gd_2O_3$/alloy can be calculated to be 0.81, 1.21, 1.64 and 1.77, respectively. In this work, the oxide films generated on the Mg-Ca and Mg-Gd alloys are consisted of CaO+MgO and $Gd_2O_3$ +MgO, so the presence of CaO and $Gd_2O_3$ can effectively improve the compactness of the oxide film. For the Mg-Y alloys, the oxide film is almost entirely composed of $Y_2O_3$, which is compact enough to resist the penetration of oxygen. The compactness of oxide film reflected by the $R_{PB}$ is consistent with the observations shown in Fig. 5 and Fig. 7.

### 4.2. Oxidation thermodynamics and the oxide-film formation process

In this work, reactive-element-rich oxide films are formed on the

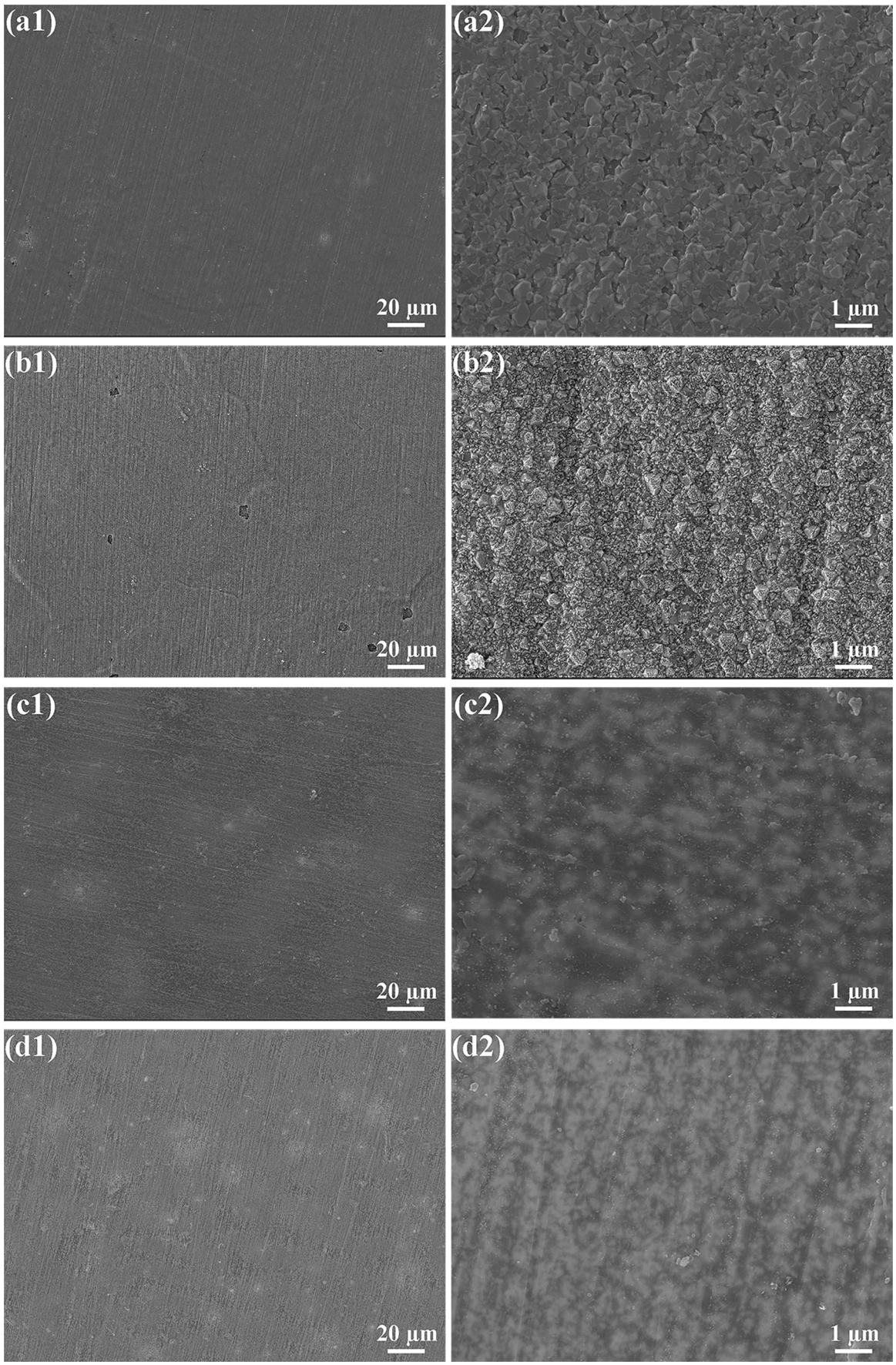


**Fig. 7.** The microstructure of the oxide films of the binary alloys after the oxidation at 500 ℃ for 100 h: (a1) (a2) C1, (b1) (b2) C2, (c1) (c2) G1, (d1) (d2) G2, (e1) (e2) G3, (f1) (f2) Y1, (g1) (g2) Y2, (h1) (h2) Y3.

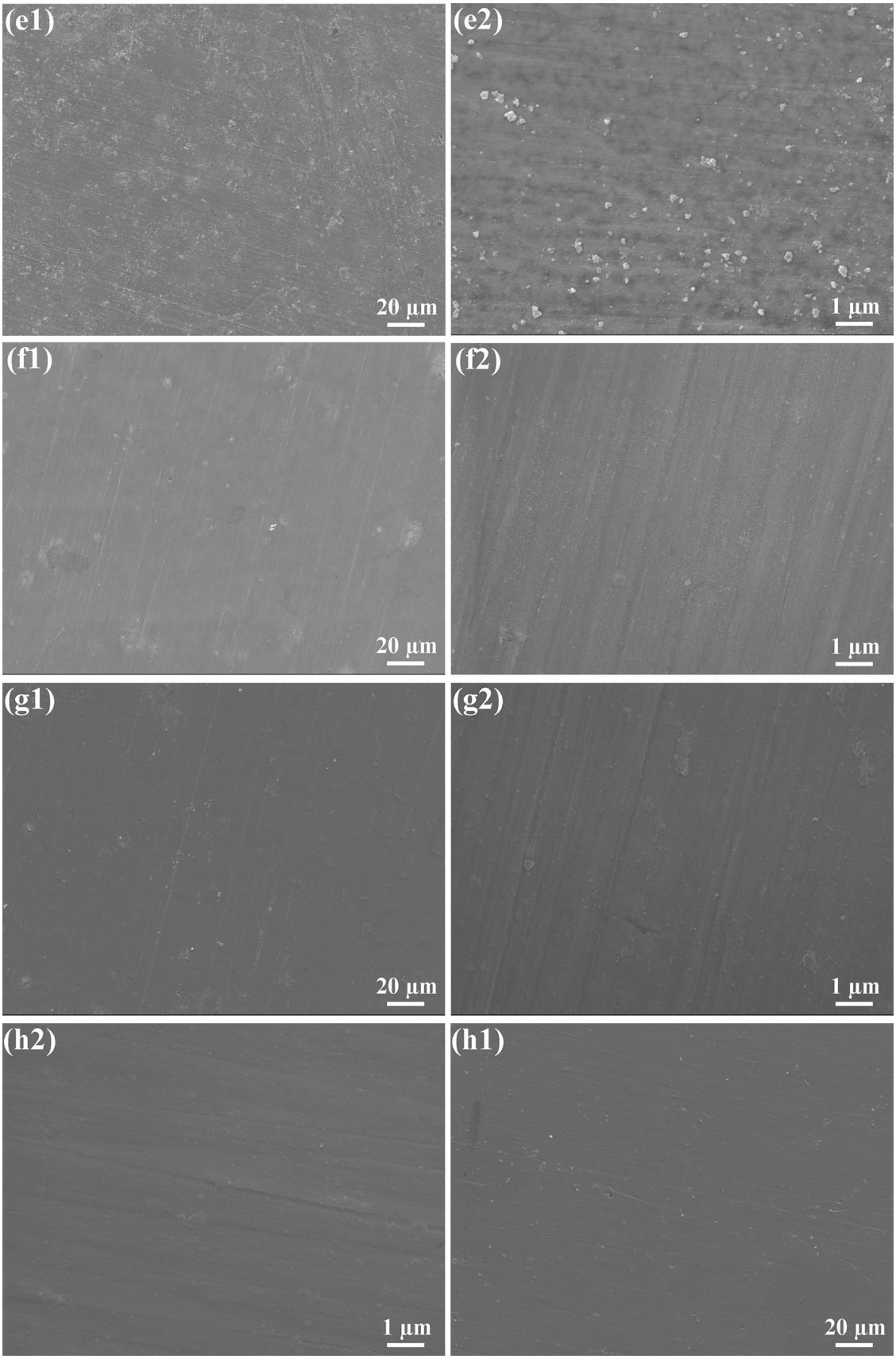


**Fig. 7.** (*continued*).

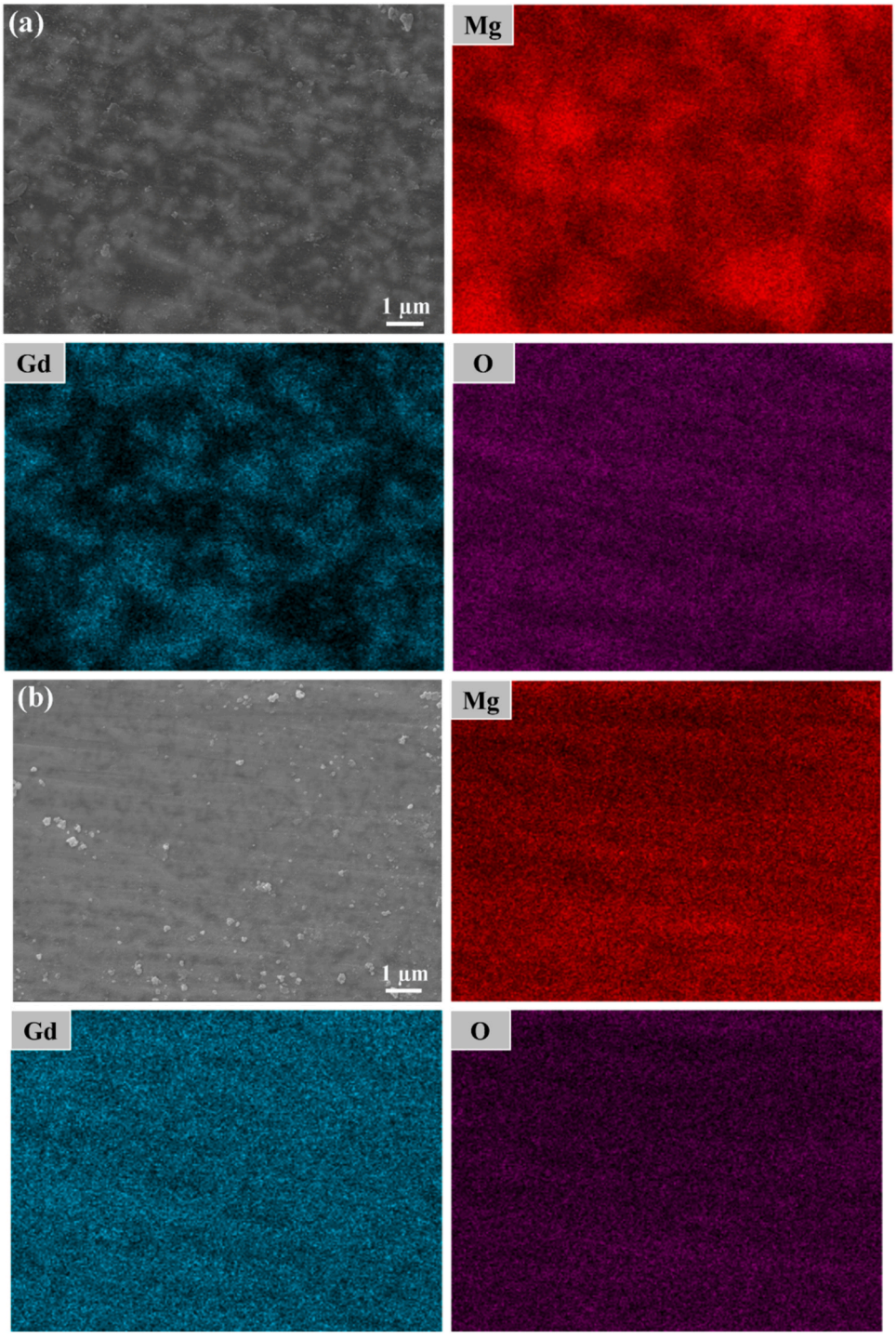


**Fig. 8.** EDS element maps of the oxide films formed on (a) G1 and (b) G3.

surface of the Mg-Ca, Mg-Gd and Mg-Y alloys, but the oxide species and their distribution are significant different among the three series alloys. The oxide films formed on the Mg-Ca alloys show distinct layered structure, and the MgO and CaO are distributed alternately (Fig. 13). The oxide films on the Mg-Gd alloys are composed of $Gd_2O_3$ and a small amount of MgO. MgO tends to be formed on the outside, while the inner layer is almost entirely composed of $Gd_2O_3$. The oxide films on the Mg-Y alloys are almost made of $Y_2O_3$. In order to better understand the formation of oxide films, a thermodynamics analysis is performed on the generation of oxides.

For the Mg-Ca alloys, the following oxidation reactions occur:

$$2\ Mg(s)+O_2(g)=2\ MgO(s) \tag{3}$$

$$2\ Ca(s)+O_2(g)=2\ CaO(s) \tag{4}$$

The standard Gibbs free energy changes of reactions (3) and (4) are calculated using Factsage software. The calculated results are shown in Eqs. (5) and (6), respectively:

$$\Delta G_1^0 = \ 1142680 + 212.80T\ [\mathrm{J/mol\ of}\ O_2] \tag{5}$$

$$\Delta G_2^0 = \ 1211560 + 207.30T\ [\mathrm{J/mol\ of}\ O_2] \tag{6}$$

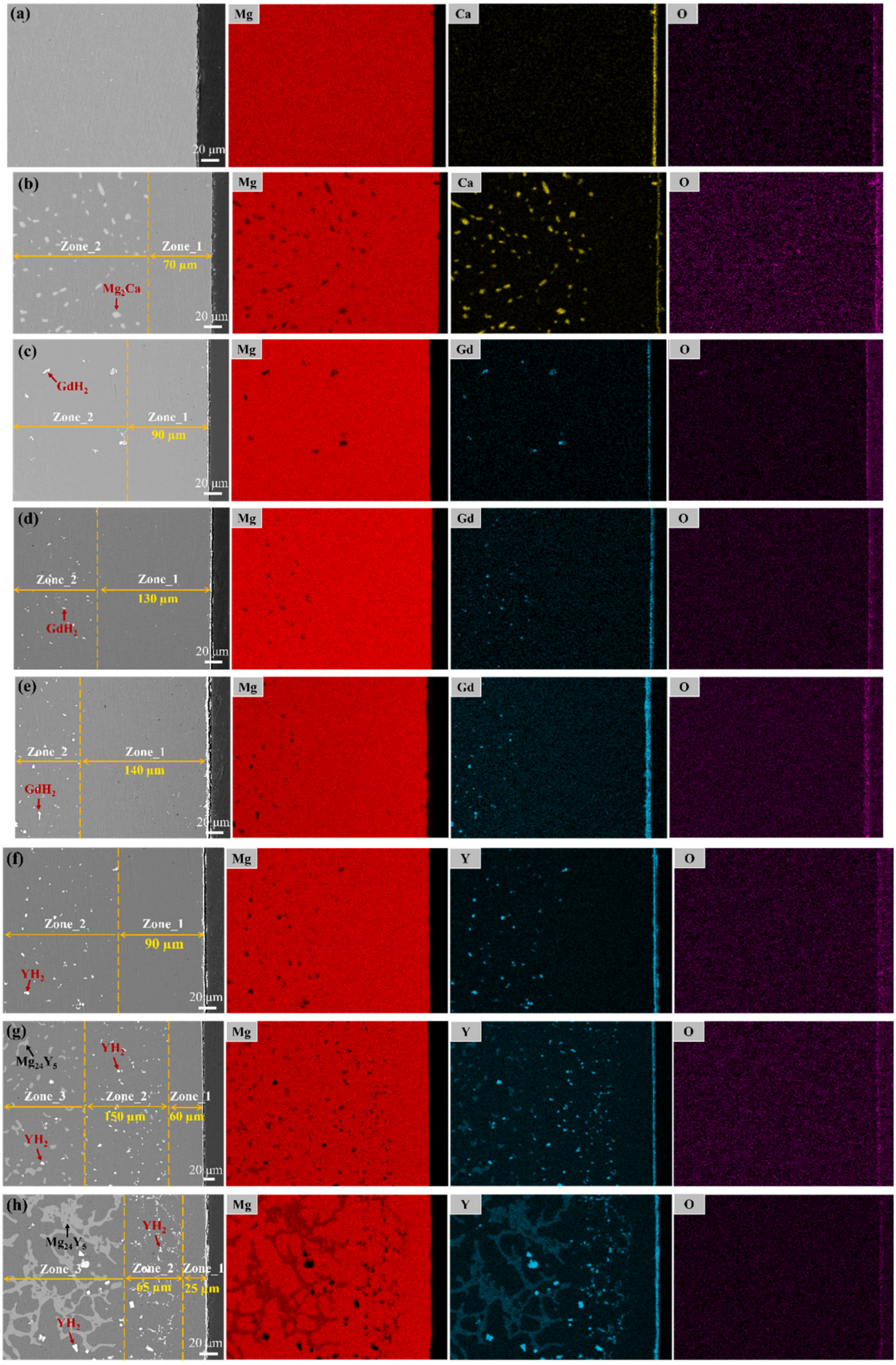


**Fig. 9.** The cross-sectional BSE images and the corresponding EDS element map of the oxide film formed on: (a) C1, (b) C2, (c) G1, (d) G2, (e) G3, (f) Y1, (g) Y2, (h) Y3.

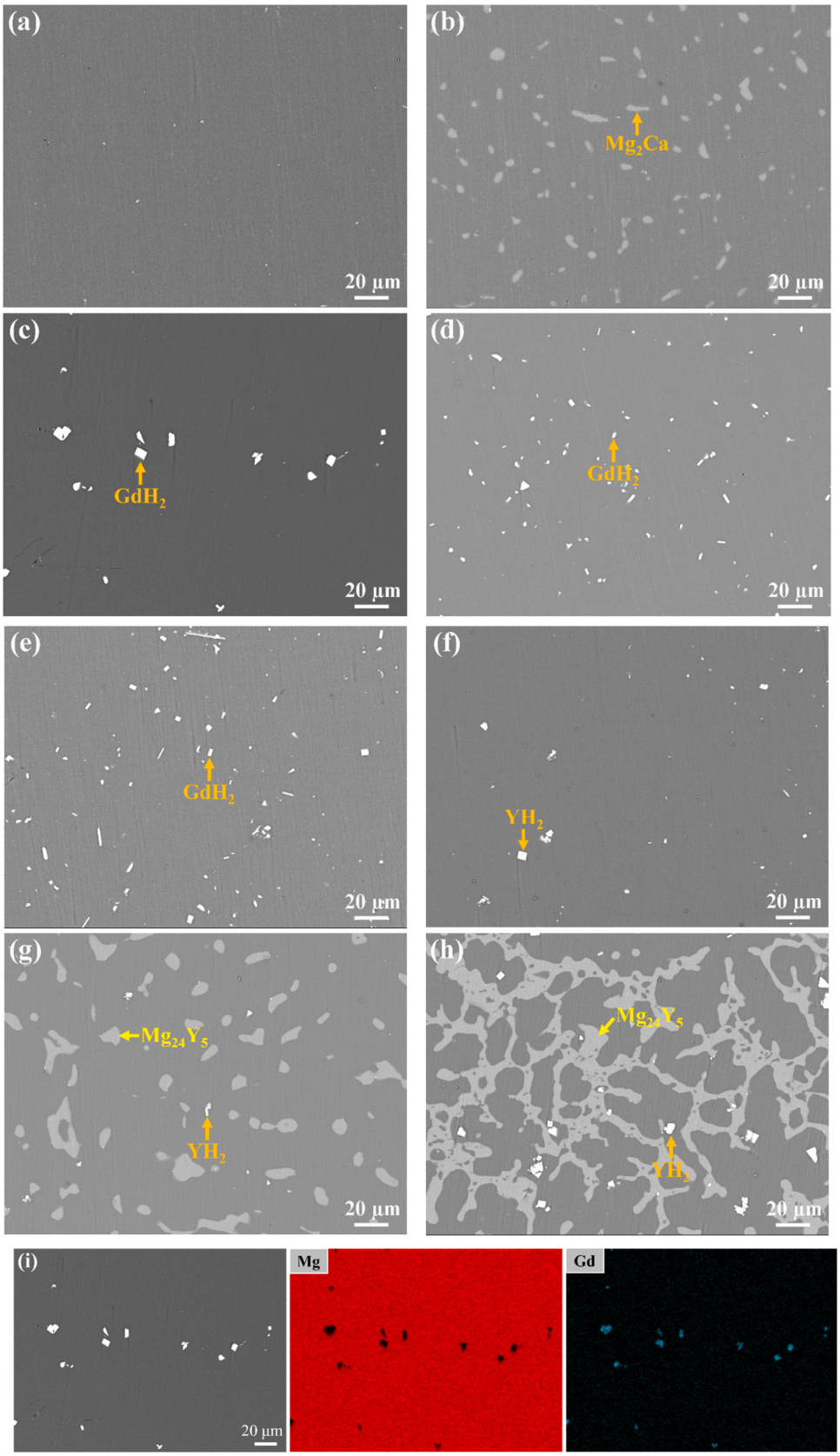


**Fig. 10.** The cross-sectional BSE images for deep matrix of the oxidized binary alloys: (a) C1, (b) C2, (c) G1, (d) G2, (e) G3, (f) Y1, (g) Y2, (h) Y3 and (i) EDS element map of G1 alloy.

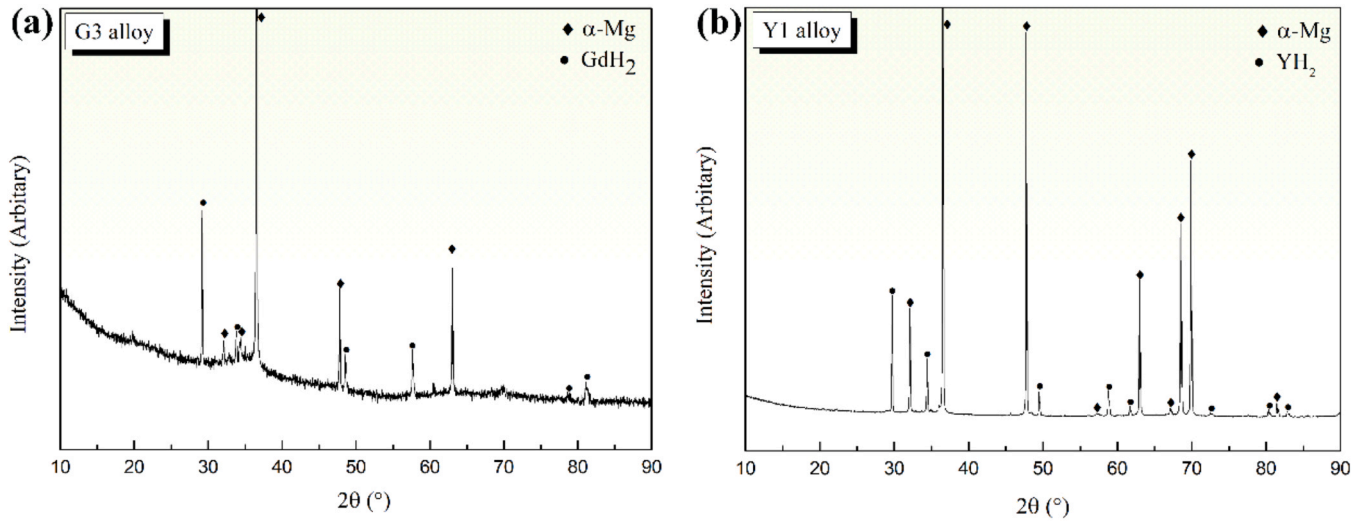


**Fig. 11.** XRD patterns of the deep matrix for the oxidized alloys: (a) G3 and (b) Y1.

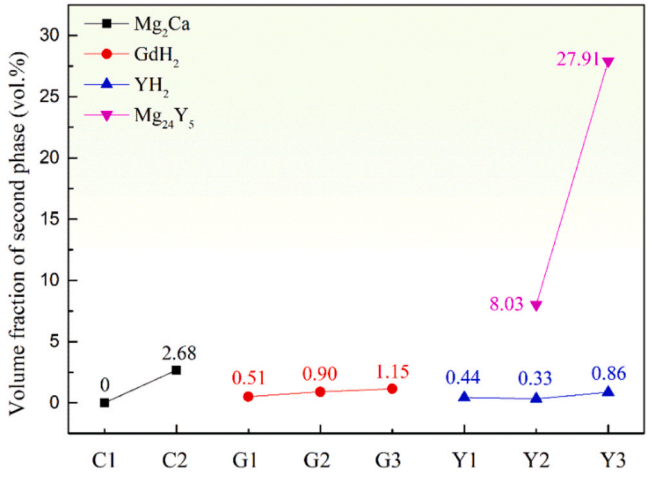


**Fig. 12.** The second phase volume fraction of deep matrix for the oxidized alloys.

The Gibbs free energy changes of reactions (3) and (4) can be calculated by the following formula:

$$\Delta G_1 = \Delta G_1^0 + RT\ln\frac{a_{MgO}^2}{a_{Mg}^2 \bullet p_{O_2}} \tag{7}$$

$$\Delta G_2 = \Delta G_2^0 + RT\ln\frac{a_{CaO}^2}{a_{Ca}^2 \bullet p_{O_2}} \tag{8}$$

Since the oxidation takes place in air, $p_{O_2} = 0.21$. Assuming that the atomic concentration of Ca is $x$, the atomic concentration of Mg is 1-$x$, and the variation of the Gibbs free energy changes of reaction (1) and (2) with the concentration of Ca can be calculated by the following equations and plotted in Fig. 15.

$$\Delta G_1(500℃) = \Delta G_1^0(500℃) + RT\ln\frac{1}{a_{Mg}^2 \bullet 0.21} = 978186 + 6426.72\ln\frac{1}{(1-x)^2 \bullet 0.21} \tag{9}$$

$$\Delta G_2(500℃) = \Delta G_2^0(500℃) + RT\ln\frac{1}{a_{Ca}^2 \bullet 0.21} = 1051317 + 6426.72\ln\frac{1}{x^2 \bullet 0.21} \tag{10}$$

For the Mg-Gd alloys, in addition to the oxidation of Mg (reaction (3)), the oxidation of Gd also occurs:

$$4/3\ Gd(s) + O_2(g) = 2/3\ Gd_2O_3(s) \tag{11}$$

The standard Gibbs free energy change for reaction (11) is as follows:

$$\Delta G_3^0 = 1158140 + 182.48T\ [J/mol\ of\ O_2] \tag{12}$$

The variation of the Gibbs free energy change with the concentration of Gd is formulated as follows, and it is also plotted in Fig. 15.

$$\Delta G_3(500℃) = \Delta G_3^0(500℃) + RT\ln\frac{1}{a_{Gd}^{4/3} \bullet p_{O_2}} = 1017083 + 6426.72\ln\frac{1}{x^{4/3} \bullet 0.21} \tag{13}$$

For the Mg-Y alloys, in addition to the oxidation of Mg (reaction (3)), the oxidation of Y also occurs:

$$4/3\ Y(s) + O_2(g) = 2/3\ Y_2O_3(s) \tag{14}$$

The standard Gibbs free energy change for reaction (14) is as follows:

$$\Delta G_4^0 = 1212930 + 187.05T\ [J/mol\ of\ O_2] \tag{15}$$

The variation of the Gibbs free energy change with the concentration of Gd is formulated as follows, and it is plotted in Fig. 15.

$$\Delta G_4(500℃) = \Delta G_4^0(500℃) + RT\ln\frac{1}{a_Y^{4/3} \bullet p_{O_2}} = 1068340 + 6426.72\ln\frac{1}{x^{4/3} \bullet 0.21} \tag{16}$$

As shown in Fig. 15, the Gibbs free energy changes of the oxidation reactions of Mg, Ca, Gd, and Y are negative, indicating that these reactions will occur spontaneously. It can be seen from Fig. 15 that there is a critical concentration of reactive element, which corresponds to the Gibbs free energy change of the Mg oxidation reaction equaling to that of oxidation reaction of Ca, Gd, and Y, respectively. When the content of reactive element is greater than the critical concentration, the Gibbs free energy changes of Ca, Gd and Y oxidation reactions are smaller than that of Mg oxidation reaction, which means that the CaO, $Gd_2O_3$ and $Y_2O_3$ are thermodynamically easier to be formed than MgO. The critical molar fractions of Ca, Gd and Y are 0.0034, 0.011 and 2.95E-5 (i.e. 0.56 wt%, 6.71 wt% and 0.01 wt%), respectively, which are calculated by the Eq. (9) (10) (13) (16). It can be seen from Fig. 9 that the second phase in the investigated alloys does not directly participate in oxidation. The second phase is firstly dissolved to release the reactive elements, which then

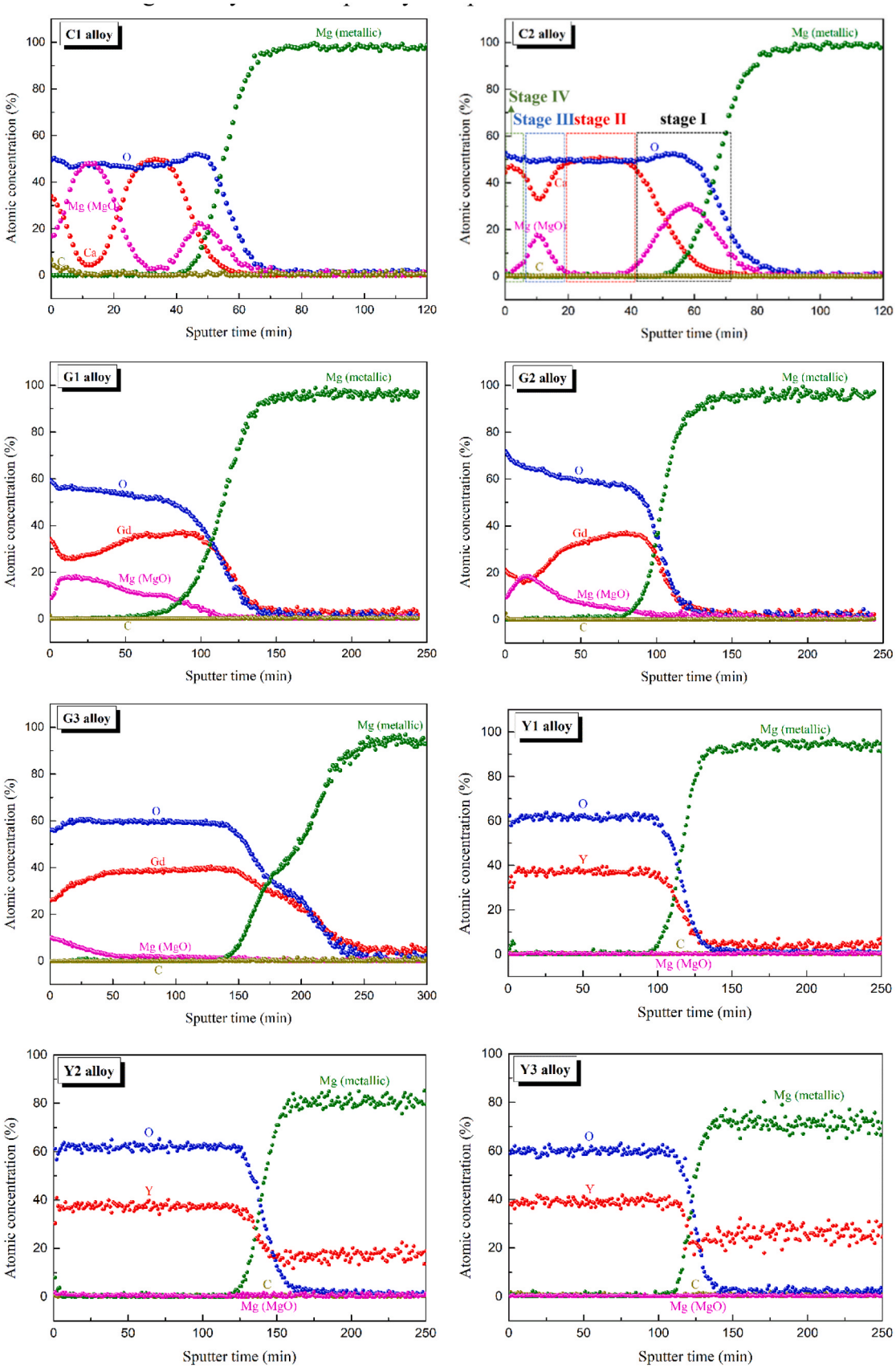


**Fig. 13.** AES patterns of the oxide film formed on the binary alloys.

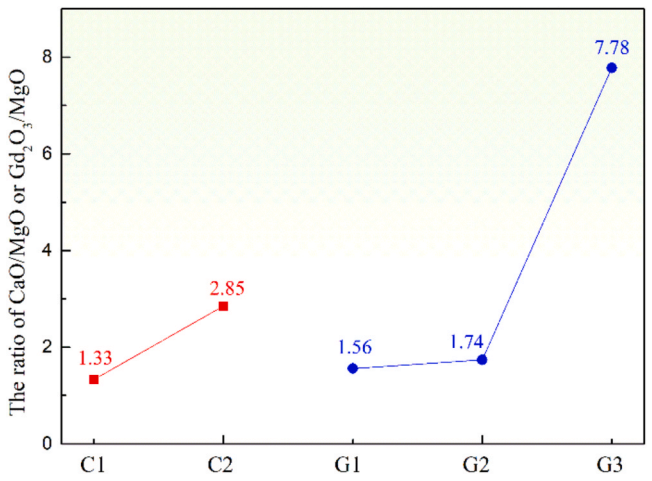


**Fig. 14.** The oxide proportion of Mg-Ca and Mg-Gd alloys.

diffuse to the surface to participate in the oxidation reaction. Therefore, the solid solubility of the reactive element in α-Mg should be taken into consideration.

For the Mg-Ca system, the solid solubility of Ca in α-Mg at 500 °C can be read from the phase diagram in Fig. 1(c), which is 0.61 wt%. For the C1 alloy, the Ca addition in the C1 alloy is 0.5 wt%, which is close to the critical concentration of Ca. Therefore, in the initial stage of oxidation, MgO and CaO are simultaneously formed on the C1 alloy. For the C2 alloy, although the Ca addition is 2.4 wt%, the maximum dissolved Ca content in α-Mg is only 0.61 wt%, owning to solid solubility limitation. Since the Ca dissolved in α-Mg is also close to the critical concentration, MgO and CaO are formed at the same time on the C2 alloy during the initial oxidation process, which is similar to the C1 alloy. Since MgO and CaO belong to NaCl structure and have Schottky defects, the ion diffusion in the oxides is dominated by cations [52–55], that is, the diffusion of $Mg^{2+}$ and $Ca^{2+}$ is significantly greater than that of $O^{2-}$. Therefore, it can be inferred that the subsequent oxidation of the Mg-Ca alloys will occur at the oxide/air interface. Taking the C2 alloy as an example, the formation process of oxide film on the Mg-Ca alloys is analyzed here. Fig. 13 shows the four-layered structure oxide film formed on the C2 alloy, and its formation process can be divided into four stages, as shown in Fig. 16. During the initial oxidation stage, as shown in Fig. 16(a), a layer of mixed oxides of MgO and CaO is formed on the C2 alloy once exposed to high-temperature air. As oxidation progresses, the metal atoms Mg and Ca at the metal/oxide interface are ionized to form $Mg^{2+}$ and $Ca^{2+}$, which enter the oxide film and diffuse to the oxide/air interface to support the oxidation. As shown in Fig. 16(b), since the diffusion of Ca atoms in α-Mg is much faster than the self-diffusion of Mg [15], an enrichment layer of Ca atoms is formed at the metal/oxide interface, where Ca atoms are ionized and diffused to the oxide/air interface to form a CaO layer. As shown in Fig. 16(c), Ca atoms at the metal/oxide interface are partially consumed, and Mg and Ca atoms are ionized and diffuse to the oxide/air interface to form a MgO+CaO mixed layer. When oxidation progresses to the fourth stage, as shown in Fig. 16 (d), Ca atoms are re-enriched at the metal/oxide interface, thus forming a CaO layer in the outermost surface on the C2 alloy. Therefore, the alternating distribution of MgO and CaO in the oxide film of the Mg-Ca alloys can be attributed to the alternating enrichment of Ca and Mg atoms at the metal/oxide interface.

For the Mg-Gd alloys, it can be seen from the phase diagram in Fig. 2 (c) that the solid solubility of Gd in α-Mg at 500 °C is 17.92 wt%, so Gd is theoretically completely dissolved in α-Mg in the G1, G2 and G3 alloys at 500 °C. As shown in Fig. 15, the critical Gd concentration is 6.71 wt%. The addition of Gd in the G1, G2 and G3 alloys is close to the critical concentration, so $Gd_2O_3$ and MgO are formed simultaneously in the initial oxidation stage, corresponding to the outermost mixed layer of $Gd_2O_3$ and MgO in Fig. 13. Lanthanide oxides are fluorite-type cubic structures ($CaF_2$ type), in which the diffusion characteristics of ions are different from these of MgO and CaO (NaCl type) [14,56]. For lanthanide oxides, metal substructures are rigid lower than one-half melting point, so 1200–1400 ℃ are required to allow metal ions to migrate in the crystal lattice [57]. However, the diffusion of $O^{2-}$ in lanthanide oxides is feasible even below 300 ℃ [56]. Therefore, the ion diffusion in $Gd_2O_3$ and $Y_2O_3$ is dominated by $O^{2-}$ [56], that is, the formation and growth of $Gd_2O_3$ and $Y_2O_3$ occur at the oxide film/metal interface. The $O^{2-}$ is diffused to the metal/oxide interface through $Gd_2O_3$, and the partial oxygen pressure at the interface gradually decreases with the progress of oxidation. $Gd_2O_3$, which has a lower decomposition pressure than MgO, is easier to form under low partial oxygen pressure [58], which explains the presence of $Gd_2O_3$ inner layer of the Mg-Gd alloys in Fig. 13.

For the Mg-Y alloys, as shown in Fig. 15, the critical Y concentration is as low as 0.01 wt%. The solid solubility of Y in α-Mg at 500 ℃ is 10.54 wt% according to the phase diagram in Fig. 3(c). At 500 ℃, the Y contents in α-Mg in the Y1, Y2 and Y3 alloys are much higher than the critical concentration. Therefore, the Gibbs free energy change of Y oxidation is much lower than that of Mg oxidation, which indicates that $Y_2O_3$ is preferentially formed compared to MgO. Similar to $Gd_2O_3$, the ion diffusion in $Y_2O_3$ is also dominated by the $O^{2-}$. Therefore, $Y_2O_3$ is continuously generated at the metal/oxide interface during the

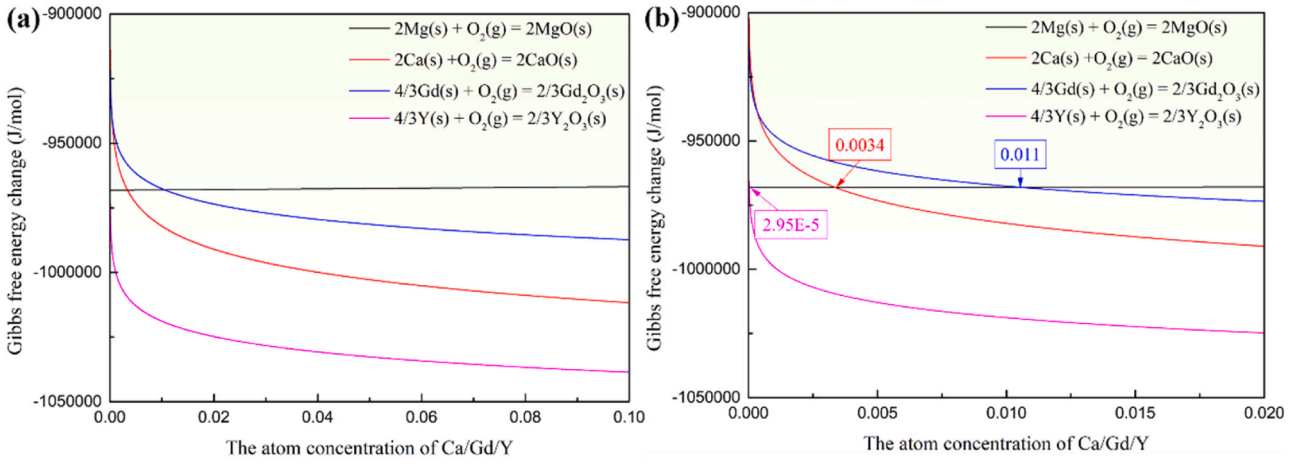


**Fig. 15.** The variation of Gibbs free energy change of oxidation reaction with the concentration of reactive elements (Ca, Gd and Y) ((b) is the magnified views of (a)).

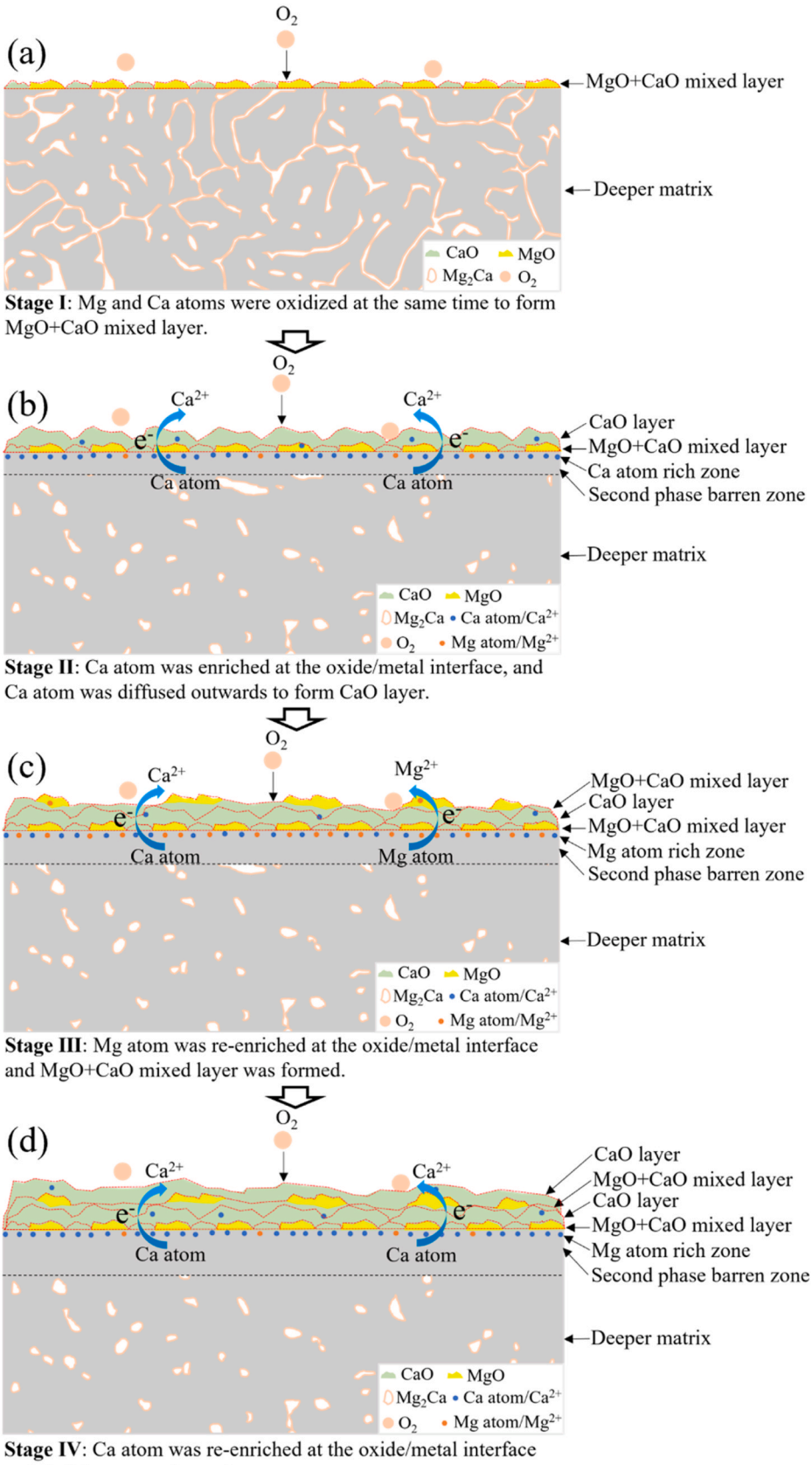


**Fig. 16.** Schematic illustration of the evolution of the multi-layered oxide film on the C2 alloy: (a) stage I, (b) stage II, (c) stage III, (d) stage IV.

subsequent oxidation process, contributing to thickening of the $Y_2O_3$ oxide film.

### 4.3. The formation process of hydride and multilayer structure in sublayer

As shown in Fig. 9, RE hydrides are formed for both Mg-Gd and Mg-Y alloys after oxidation. A multilayer structure in sublayer is also exhibited for the Y2 and Y3 alloys. Taking the Y3 alloy as an example, the formation mechanism of hydride $YH_2$ and multilayer structure in sublayer are clarified. First of all, the formation of hydrides is discussed. The cuboid RE hydrides are sometimes encountered in as-cast Mg-RE alloys and observed more frequently for the alloys subjected to solution treatment or annealing at high temperature [48,50]. RE elements have a strong ability to adsorb hydrogen and can quickly form RE hydrides. The thermal decomposition temperature of RE hydrides is above 1000 ℃ [49]. Mg can also react with $H_2$ to form $MgH_2$, but its thermal decomposition temperature is about 290 ℃ [50]. The oxidation temperature in this work is 500 ℃, which explains the absent of $MgH_2$ in the Mg-Gd and Mg-Y alloys. There are some speculations about the source of hydrogen for the formation of RE hydrides according to previous research [48,51,60]: (I) hydrogen that dissolved inside the metal [50]; (II) the external environment: (1) the Mg reacts with water to form hydrogen during the grinding process, which reacts with RE to form hydride on the surface [47,59]; (2) water vapor in air is decomposed on the surface at high temperature to produce hydrogen, which diffuses into the metal interior [49,60]. As shown in Fig. 9(g)-(h) and Fig. 12, the amount of $YH_2$ in zone_2 is much higher than that of $YH_2$ in zone_3 for the Y2 and Y3 alloys. Therefore, the hydrogen in this work mainly comes from the external environment, in which water vapor is decomposed to produce the hydrogen during the high-temperature oxidation process. In addition, it can be seen that $YH_2$ in zone_2 of the Y2 and Y3 alloys is distributed along grain boundaries. Wu [60] also found the distribution of RE hydride along grain boundaries in Mg-Gd-Y-Zn-Zr alloys, and proposed that H mainly diffuses along grain boundaries.

Taking the Y2 alloy as an example, the formation of RE hydrides and the formation process of multilayer structure of sublayer are shown in Fig. 17. Firstly, the water vapor on the surface is decomposed to produce hydrogen, which is then dissociative adsorbed by the surface to generate H atoms. The H atoms diffuse inward to reach the front of the $Mg_{24}Y_5$ phase distributed along the grain boundaries in the inner layer, resulting in the decomposition of the $Mg_{24}Y_5$ phase and the formation of the $YH_2$ phase. In addition, as shown in Fig. 9(g) (h), the $YH_2$ phase is dissolving near the zone_1/zone_2 interface, which releases Y atoms that continuously diffuse through zone_1 toward the surface to participate in the formation of oxide films. This also implies that the zone_1/zone_2 interface moves forward gradually with the progress of oxidation. It is

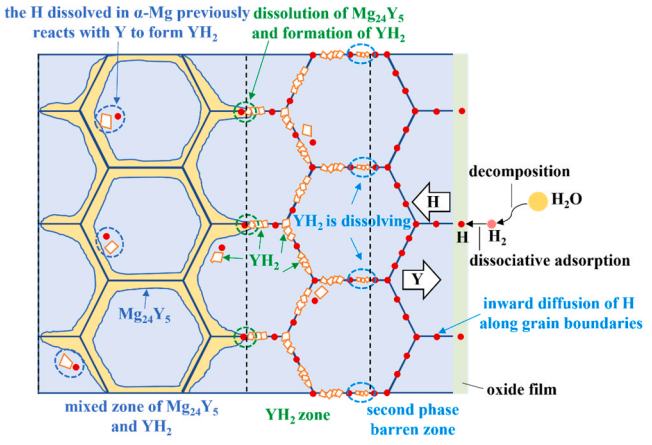


**Fig. 17.** Schematic illustration of the formation of RE hydrides and the multilayer structure in sublayer of the Y2 alloy.

worth noting that there is no second phase in zone_1. The Y atoms in zone_1 are constantly diffusing outward, so there is a chemical potential gradient of Y in zone_1. The chemical potential gradient of Y prevents the $YH_2$ phase from effectively nucleating/growing in zone_1, which is also the driving force for the continuous dissolution of the $YH_2$ phase near zone_1/zone_2 interface. A small number of coarse $YH_2$ phase is present in zone_3, near the $Mg_{24}Y_5$ phase along grain boundaries. The source of the H for the $YH_2$ phase in zone_3 may be the hydrogen dissolved previously in the alloy, which reacts with Y at high temperatures to form $YH_2$. The external H is mainly captured by the $Mg_{24}Y_5$ phase at the zone_1/zone_2 interface and cannot be effectively diffused into deeper matrix, which can also be supported by the large number of $YH_2$ phase formed in zone_2. Therefore, the hydrogen source of the $YH_2$ phase is proposed to come both from the decomposition of external water vapor and the hydrogen dissolved previously in the metal.

### 4.4. Factors of the parabolic rate constant $k_p$

Chatterjee [61] established a kinetic model of the high-temperature oxidation for nickel-base alloys. The parabolic rate constant $k_p$ is correlated with the partial pressure gradient of oxygen across the oxide film and diffusion coefficients of cation and anion in this model:

$$k_p = \int_{P_{O_2}(I)}^{P_{O_2}(II)} \left( \frac{\alpha D_M^*}{f_M} + \frac{D_O^*}{f_O} \right) d\mathrm{Ln} P_{O_2} \tag{17}$$

where $P_{O_2}(I)$ and $P_{O_2}(II)$ are the partial pressures of oxygen at the metal/oxide and oxide/gas interfaces, $\alpha$ is a stoichiometry coefficient, $D_M^*$ and $D_O^*$ are the tracer diffusivities of cations and anions in the oxide, $f_M$ and $f_O$ are correlation factors for self-diffusion.

The parabolic rate constant $k_p$ is determined by both thermodynamics (driving force) and kinetics (diffusion coefficients). The high-temperature oxidation of pure Mg was investigated by Ma [62], and $k_p$ was described based on CALPHAD-type thermodynamic and kinetic descriptions:

$$k_p = \frac{\Delta\mu_O}{RT}(D_{Mg}^* + D_O^*) \tag{18}$$

where $\Delta\mu_O$ is the difference of chemical potential of oxygen in Mg oxide. $D_i^*$ denotes the tracer diffusion coefficient of component i in oxide layer.

The above two models correspond to alloy (Ni-based alloys) and pure metal (pure Mg). As there is a lack of research on oxidation kinetic model of Mg-based alloys, the oxidation kinetics of Mg alloy is discussed in combination with the above two models. According to the two models, it can be seen that $k_p$ is positively correlated with the oxygen concentration gradient across the oxide film and the diffusion coefficients of cation and anion. The oxygen concentration gradient across the oxide film can be reflected by the difference of the oxygen partial pressure at the oxide film/gas interface and the oxide film/metal interface.

As discussed in Section 4.1, the growth of CaO and MgO on Mg-Ca alloys is dominated by outward diffusion of cations due to the NaCl structure. However, $Y_2O_3$ and $Gd_2O_3$ are dominated by the inward diffusion of $O^{2-}$ due to the fluorite-type cubic structure. According to Fig. 4 and Table 2 in Section 3.2, the $k_p$ of Mg-Ca alloys is significantly lower than that of Mg-Gd and Mg-Y alloys, which is speculated to be caused by the slower diffusion of $Ca^{2+}$ and $Mg^{2+}$ in the CaO+MgO compared to that of $O^{2-}$ in $Gd_2O_3/Y_2O_3$ under the oxidation at 500 °C. Nevertheless, the current diffusion research of oxides is mainly aimed at temperature above 1000 °C, more work should be conducted at the low temperature range. In addition, Fig. 4 and Table 2 also show that $k_p$ increases with the increment of the content of reactive element. According to the above models, the two factors, oxygen concentration gradient and ion diffusion coefficient, may be affected by the content of reactive element, which induced the occurring of this phenomenon.

On the one hand, a higher content of reactive element addition in-

dicates more reactive element at the oxide/metal interface. Higher amount of oxygen at the interface will be captured by the reactive element and the oxygen partial pressure is reduced. So the oxygen concentration gradient across the oxide film is increased which elevates $k_p$. On the other hand, the increased content of reactive elements may enhance the diffusion of ions across oxide. Early studies showed that both lattice and grain boundary diffusion contributed to the growth of oxide [63]. Therefore, the diffusion coefficient $D$ could be expressed as [64]:

$$D = D_L(1 \quad f) + D_B f \tag{19}$$

where $D_L$ and $D_B$ denote the lattice and grain boundary diffusion coefficients, respectively, and $f$ is the fraction of the diffusion along grain boundaries. Assuming a cubic shaped grain, the fraction $f$ can be calculated as [63]:

$$f = \frac{2\delta}{a} \tag{20}$$

where $\delta$ is the grain boundary width and $a$ is the oxide grain size. Therefore, the contribution of grain boundary diffusion increases with the reduction of grain size.

Growth of oxide film at temperature up to one-half melting point of oxide is dominantly dependent on grain boundary diffusion rather than lattice diffusion [63]. Therefore, the ion diffusion in the oxide film is dominated by grain boundary diffusion in this work. For the Mg-Ca alloys, the oxide grain size of the C2 alloy is significantly smaller than that of the C1 alloy (Fig. 7). So the oxide film on the C2 alloy exhibits higher ion diffusion coefficient, and the larger $k_p$ of the C2 alloy is obtained. For the Mg-Gd and Mg-Y alloys, the oxide grain size is hardly observed from the microstructure in Fig. 7. However, it can be speculated that the grain size of oxide also decreases with the increased content of reactive elements. This is probably caused by the greater chance of nucleation with the higher amount of reactive element at the oxide/metal interface.

## 5. Conclusion

The long-term oxidation behavior of the Mg-X (X = Ca/Gd/Y) binary alloys was investigated using a semi in-situ oxidation test. The structures of the oxide film and the substrate were analyzed using SEM/EDS, XRD and AES. The oxidation behavior was clarified based on thermodynamics and kinetics. The results are summarized as follows:

1. Reactive elements Ca, Gd and Y effectively improved the high-temperature oxidation resistance of Mg. This was attributed to the compact and crack-free oxide films formed on the surface of these binary alloys, which isolated the metal matrix from contacting with air.
2. Composite oxide films of CaO+MgO and $Gd_2O_3$ + MgO were formed on the surface of the Mg-Ca and Mg-Gd alloys, respectively, while a single $Y_2O_3$ oxide film on the Mg-Y alloys was observed. The critical concentrations of reactive elements were calculated based on thermodynamics and can be used as the criteria to judge the oxides formation priority.
3. The oxide films of the Mg-Ca alloys exhibited a four-layered structure, in which MgO and CaO were distributed alternately. This is suggested to be caused by the alternating enrichment of Ca and Mg atoms at the metal/oxide interface.
4. During the oxidation process, the water vapor in the furnace was decomposed on the surface of the sample to produce H, which diffused along the grain boundary into the metal and participated in the formation of RE hydrides.
5. There was a second phase depleted zone in sublayer of oxide film, where the RE was continuously diffused to the surface. The chemical potential gradient of the RE in this zone prevented the second phase from effectively nucleating/growing, and it was also responsible for the dissolution of RE hydrides in the deeper matrix.

## CRediT authorship contribution statement

**Jiajia Wu:** Writing – original draft, Investigation, Methodology, Formal analysis, Data curation. **Yuan Yuan**: Conceptualization, Writing – review & editing, Supervision, Project administration, Funding acquisition. **Tao Chen:** Formal analysis, Data curation. **Aitao Tang**: Resources. **Liang Wu**: Resources. **Dajian Li:** Investigation, Resources, Data curation. **Martin Steinbrück:** Resources, Writing – review & editing. **Fusheng Pan:** Supervision, Project administration, Funding acquisition.

## Declaration of Competing Interest

The authors declare that they have no known competing financial interests or personal relationships that could have appeared to influence the work reported in this paper.

## Data availability

The raw/processed data required to reproduce these findings are available on request.

## Acknowledgements

This work is financially supported by National Key R&D Program of China (2021YFB3701100) and National Natural Science Foundation of China (52171100, 51971044). Scientific Research Foundation for the Returned Chinese Scholars of Chongqing Human Resources and Social Security Bureau (cx2021109). The technology support by Testing Center of Chongqing University and Karlsruhe Nano Micro Facility (KNMF) of KIT is greatly acknowledged.

## References

[1] Q.Y. Tan, A. Atrens, N. Mo, M.X. Zhang, Oxidation of magnesium alloys at elevated temperatures in air: a review, Corros. Sci. 112 (2016) 734–759.
[2] F. Czerwinski, The reactive element effect on high-temperature oxidation of magnesium, Int. Mater. Rev. 60 (2015) 264–296.
[3] F. Czerwinski, Controlling the ignition and flammability of magnesium for aerospace applications, Corros. Sci. 86 (2014) 1–16.
[4] A. Atrens, Z. Shi, S.U. Mehreen, S. Johnston, G.L. Song, X.H. Chen, F.S. Pan, Review of Mg alloy corrosion rates, J. Magnes. Alloy 8 (2020) 989–998.
[5] F.H. Froes, Advanced metals for aerospace and automotive use, Mater. Sci. Eng. A Struct. 184 (1994) 119–133.
[6] Q.Y. Tan, N. Mo, C.L. Lin, Y.T. Zhao, Y. Yin, B. Jiang, F.S. Pan, A. Atrens, H. Huang, M.X. Zhang, Generalisation of the oxide reinforcement model for the high oxidation resistance of some Mg alloys micro-alloyed with Be, Corros. Sci. 147 (2019) 357–371.
[7] F. Czerwinski, Overcoming barriers of magnesium ignition and flammability, Adv. Mater. Process 172 (2014) 28–31.
[8] C.L. Cheng, Q. Lan, A. Wang, Q.C. Le, F. Yang, X.Q. Li, Effect of Ca additions on ignition temperature and multi-stage oxidation behavior of AZ80, Metals 8 (2018) 766.
[9] S.Z. Zhao, H. Zhou, T. Zhou, Z.H. Zhang, P.Y. Lin, L.Q. Ren, The oxidation resistance and ignition temperature of AZ31 magnesium alloy with additions of La2O3 and La, Corros. Sci. 67 (2013) 75–81.
[10] F. Czerwinski, Oxidation characteristics of magnesium alloys, JOM 64 (2012) 1477–1483.
[11] C.L. Cheng, X.Q. Li, Q.C. Le, R.Z. Guo, Q. Lan, J.Z. Cui, Effect of REs (Y, Nd) addition on high temperature oxidation kinetics, oxide layer characteristic and activation energy of AZ80 alloy, J. Magnes. Alloy 8 (2020) 1281–1295.
[12] X.W. Yu, S.J. Shen, B. Jiang, Z.T. Jiang, H. Yang, F.S. Pan, The effect of the existing state of Y on high temperature oxidation properties of magnesium alloys, Appl. Surf. Sci. 370 (2016) 357–363.
[13] X.W. Yu, B. Jiang, H. Yang, Q.S. Yang, X.S. Xia, F.S. Pan, High temperature oxidation behavior of Mg-Y-Sn, Mg-Y, Mg-Sn alloys and its effect on corrosion property, Appl. Surf. Sci. 353 (2015) 1013–1022.
[14] J.J. Wu, Y. Yuan, L. Yang, T. Chen, D.J. Li, L. Wu, B. Jiang, M. Steinbrück, F.S. Pan, The oxidation behavior of Mg-Er binary alloys at 500 °C, Corros. Sci. 195 (2022), 109961.

[15] J.J. Wu, Y. Yuan, X.W. Yu, T. Chen, D.J. Li, L. Wu, B. Jiang, A. Atrens, F.S. Pan, The high-temperature oxidation resistance properties of magnesium alloys alloyed with Gd and Ca, J. Mater. Sci. 56 (2021) 8745–8761.
[16] Q.Y. Tan, N. Mo, B. Jiang, F.S. Pan, A. Atrens, M.X. Zhang, Combined influence of Be and Ca on improving the high-temperature oxidation resistance of the magnesium alloy Mg-9Al-1Zn, Corros. Sci. 122 (2017) 1–11.
[17] L.Y. Wu, H.T. Li, Effect of selective oxidation on corrosion behavior of Mg–Gd–Y–Zn–Zr alloy, Corros. Sci. 142 (2018) 238–248.
[18] K. Hagihara, T. Okamoto, H. Izuno, M. Yamasaki, M. Matsushita, T. Nakano, Y. Kawamura, Plastic deformation behavior of 10H-type synchronized LPSO phase in a Mg–Zn–Y system, Acta Mater. 109 (2016) 90–102.
[19] Y.Q. Chi, J.W. Liu, Z.J. Zhou, S.Z. Wu, W.Q. Liu, M.Y. Zheng, Investigation on the microstructure, texture and mechanical properties of Mg-Gd-Y(-Zn)-Zr alloys under indirect extrusion, J. Alloy Compd. 943 (2023), 169061.
[20] E. Oñorbe, G. Garcés, P. Pérez, P. Adeva, Effect of the LPSO volume fraction on the microstructure and mechanical properties of Mg-$Y_{2X}$-$Zn_X$ alloys, J. Mater. Sci. 47 (2012) 1085–1093.
[21] K. Hagihara, A. Kinoshita, Y. Fukusumi, M. Yamasaki, Y. Kawamura, High-temperature compressive deformation behavior of Mg97Zn1Y2 extruded alloy containing a long-period stacking ordered (LPSO) phase, Mater. Sci. Eng. A Struct. 560 (2013) 71–79.
[22] S.I. Inoue, M. Yamasaki, Y. Kawamura, Oxidation behavior and incombustibility of molten Mg-Zn-Y alloys with Ca and Be addition, Corros. Sci. 149 (2019) 133–143.
[23] X. Yu, B. Jiang, J.J. He, B. Liu, Z.T. Jiang, F.S. Pan, Effect of Zn addition on the oxidation property of Mg-Y alloy at high temperatures, J. Alloy Compd. 687 (2016) 252–262.
[24] S.I. Inoue, M. Yamasaki, Y. Kawamura, Formation of an incombustible oxide film on a molten Mg-Al-Ca alloy, Corros. Sci. 122 (2017) 118–122.
[25] T.W. Lee, H.W. Park, H. Lim, S.K. Kim, S.H. Lim, Microstructural characterization of oxide layers in CaO added AZ31 Mg alloy, J. Alloy Compd. 714 (2017) 397–408.
[26] J.K. Lee, S.K. Kim, Effect of CaO composition on oxidation and burning behaviors of AM50 Mg alloy, Trans. Nonferrous Met. Soc. 21 (2011) s23–s27.
[27] D.B. Lee, High temperature oxidation of AZ31+0.3wt%Ca and AZ31+0.3wt%CaO magnesium alloys, Corros. Sci. 70 (2013) 243–251.
[28] M. Zubair, M. Felten, B. Hallstedt, M. Vega Paredes, L. Abdellaoui, R. Bueno Villoro, M. Lipinska Chwalek, N. Ayeb, H. Springer, J. Mayer, B. Berkels, D. Zander, S. Korte-Kerzel, C. Scheu, S. Zhang, Laves phases in Mg-Al-Ca alloys and their effect on mechanical properties, Mater. Des. 225 (2023), 111470.
[29] M. Zubair, S. Sandlöbes-Haut, M. Lipińska-Chwałek, M.A. Wollenweber, C. Zehnder, J. Mayer, J.S.K.L. Gibson, S. Korte Kerzel, Co-deformation between the metallic matrix and intermetallic phases in a creep-resistant Mg-3.68Al-3.8Ca alloy, Mater. Des. 210 (2021), 110113.
[30] D. Andre, M. Freund, U. Rehman, W. Delis, M. Felten, J. Nowak, C. Tian, M. Zubair, L. Tanure, L. Abdellaoui, H. Springer, J.P. Best, D. Zander, G. Dehm, S. Sandlöbes-Haut, S. Korte-Kerzel, Metallographic preparation methods for the Mg based system Mg-Al-Ca and its Laves phases, Mater. Charact. 192 (2022), 112187.
[31] D. Amberger, P. Eisenlohr, M. Göken, Microstructural evolution during creep of Ca-containing AZ91, Mater. Sci. Eng. A 510–511 (2009) 398–402.
[32] A.A. Luo, B.R. Powell, M.P. Balogh, Creep and microstructure of magnesium-aluminum-calcium based alloys, Met. Mater. Trans. A 33 (2002) 567–574.
[33] B.S. You, W.W. Park, I.S. Chung, The effect of calcium additions on the oxidation behavior in magnesium alloys, Scr. Mater. 42 (2000) 1089–1094.
[34] S.L. Cheng, G.C. Yang, J.F. Fan, Y.J. Li, Y.H. Zhou, Effect of Ca and Y additions on oxidation behavior of AZ91 alloy at elevated temperatures, Trans. Nonferrous Met. Soc. 19 (2009) 299–304.
[35] F. Li, W.Y. Peh, V. Nagarajan, M.K. Ho, A. Danno, B.W. Chua, M.J. Tan, Development of non-flammable high strength AZ91+Ca alloys via liquid forging and extrusion, Mater. Des. 99 (2016) 37–43.
[36] Q.Y. Tan, N. Mo, B. Jiang, F.S. Pan, A. Atrens, M.X. Zhang, Oxidation resistance of Mg–9Al–1Zn alloys micro-alloyed with Be, Scr. Mater. 115 (2016) 38–41.
[37] Q.Y. Tan, N. Mo, C.L. Lin, B. Jiang, F.S. Pan, H. Huang, A. Atrens, M.X. Zhang, Improved oxidation resistance of Mg-9Al-1Zn alloy microalloyed with 60 wt ppm Be attributed to the formation of a more protective (Mg,Be)O surface oxide, Corros. Sci. 132 (2018) 272–283.
[38] Z.L. Ning, W.Z. Liang, F.Y. Cao, J.F. Sun, The effect of Y on the oxidation of Mg-Zn-Zr alloys, Int J. Mod. Phys. B 23 (2009) 796–801.
[39] X.M. Wang, X.Q. Zeng, Y. Zhou, G.S. Wu, S.S. Yao, Y.J. Lai, Early oxidation behaviors of Mg–Y alloys at high temperatures, J. Alloy Compd. 460 (2008) 368–374.
[40] X.M. Wang, W.D. Wu, Y.J. Tang, X.Q. Zeng, S.S. Yao, Early high temperature oxidation behaviors of Mg–10Gd–3Y alloys, J. Alloy Compd. 474 (2009) 499–504.
[41] S.I. Inoue, M. Yamasaki, Y. Kawamura, Classification of high-temperature oxidation behavior of Mg-1 at% X binary alloys and application of proposed taxonomy to nonflammable multicomponent Mg alloys, Corros. Sci. 174 (2020), 108858.
[42] D.S. Aydin, Z. Bayindir, M. Hoseini, M.O. Pekguleryuz, The high temperature oxidation and ignition behavior of Mg-Nd alloys part I: the oxidation of dilute alloys, J. Alloy Compd. 569 (2013) 35–44.
[43] X.W. Yu, B. Jiang, J.J. He, B. Liu, F.S. Pan, Oxidation resistance of Mg-Y alloys at elevated temperatures and the protection performance of the oxide films, J. Alloy Compd. 749 (2018) 1054–1062.
[44] M.D. López, C.J. Múnez, M. Carboneras, P. Rodrigo, M.D. Escalera, E. Otero, Influence of temperature on oxidation behaviour of ZE41 magnesium alloy, J. Alloy Compd. 491 (2010) 131–136.
[45] D.S. Aydin, Z. Bayindir, M.O. Pekguleryuz, High temperature oxidation behavior of hypoeutectic Mg-Sr binary alloys: the role of the two-phase microstructure and the surface activity of Sr, Adv. Eng. Mater. 17 (2015) 697–708.
[46] L.Y. Wu, Y.A. Li, Y.L. Cheng, L.H. Feng, F.L. Jiang, G. Chen, J. Teng, D.F. Fu, H. Zhang, Microstructure evolution and corrosion resistance improvement of Mg–Gd–Y–Zn–Zr alloys via surface hydrogen treatment, Corros. Sci. 191 (2021), 109746.
[47] Q.M. Peng, Y.D. Huang, J. Meng, Y.D. Li, K.U. Kainer, Strain induced GdH2 precipitate in Mg–Gd based alloys, Intermetallics 19 (2011) 382–389.
[48] S.M. Zhu, J.F. Nie, M.A. Gibson, M.A. Easton, On the unexpected formation of rare earth hydrides in magnesium–rare earth casting alloys, Scr. Mater. 77 (2014) 21–24.
[49] K.Y. Zheng, J. Dong, X.Q. Zeng, W.J. Ding, Microstructural characterisation of as cast and homogenised Mg–Gd–Nd–Zr alloys, Mater. Sci. Technol. 24 (2013) 320–326.
[50] Y.L. Yang, L.M. Peng, P.H. Fu, B. Hu, W.J. Ding, Identification of NdH2 particles in solution-treated Mg-2.5%Nd (wt%) alloy, J. Alloy Compd. 485 (2009) 245–248.
[51] C.L. Cheng, Q.C. Le, D.J. Li, W.X. Hu, T. Wang, R.Z. Guo, C.L. Hu, Effect of Y on high-temperature oxidation behavior and products of AZ80 alloy, Mater. Chem. Phys. 269 (2021), 124732.
[52] B.J. Wuensch, W.C. Steele, T. Vasilos, Cation self-diffusion in single-crystal MgO, J. Chem. Phys. 58 (1973) 5258–5266.
[53] D.K. Fisler, R.T. Cygan, Diffusion of Ca and Mg in calcite, Am. Miner. 84 (1999) 1392–1399.
[54] J.H. Park, T.F. Kassner, CaO insulator coatings and self-healing of defects on V-Cr-Ti alloys in liquid lithium system, J. Nucl. Mater., 233- 237 (1996) 476–481.
[55] D.B. Lee, L.S. Hong, Y.J. Kim, Effect of Ca and CaO on the high temperature oxidation of AZ91D Mg alloys, Mater. Trans. 49 (2008) 1084–1088.
[56] G.Y. Adachi, N. Imanaka, The binary rare earth oxides, Chem. Rev. 98 (1998) 1479–1514.
[57] R.G. Haire, L. Eyring, Handbook on the Physics and Chemistry of Rare Earths, 18, North-Holland, Amsterdam, 1994.
[58] J.F. Fan, G.C. Yang, Y.H. Zhou, Y.H. Wei, B.S. Xu, Selective oxidation and the third-element effect on the oxidation of Mg-Y alloys at high temperatures, Met. Mater. Trans. A 40 (2009) 2184–2189.
[59] W. Gan, Y. Huang, L. Yang, K.U. Kainer, M. Jiang, H.G. Brokmeier, N. Hort, Identification of unexpected hydrides in Mg–20 wt% Dy alloy by high-brilliance synchrotron radiation, J. Appl. Crystallogr 45 (2011) 17–21.
[60] L.Y. Wu, Y.A. Li, Y.L. Cheng, L.H. Feng, F.L. Jiang, G. Chen, J. Teng, D.F. Fu, H. Zhang, Microstructure evolution and corrosion resistance improvement of Mg-Gd-Y-Zn-Zr alloys via surface hydrogen treatment, Corros. Sci. 191 (2021), 109746.
[61] A. Chatterjee, S. Srikanth, S. Sanyal, L. Krishna, K. Anand, P.R. Subramanian, Kinetic modeling of high temperature oxidation of Ni-base alloys, Comput. Mater. Sci. 50 (2011) 811–819.
[62] S. Ma, F.Z. Xing, N. Ta, L.J. Zhang, Kinetic modeling of high-temperature oxidation of pure Mg, J. Magnes. Alloy 8 (2020) 819–831.
[63] W. Smeltzer, The influence of short-circuit grain boundary diffusion on the growth of oxide layers on metals, Mater. Sci. Forum 29 (1988) 151–172.
[64] W. Smeltzer, Oxidation of an aluminum-3 per cent magnesium alloy in the temperature range 200 ℃-550 ℃, J. Electrochem. Soc. 105 (1958) 67–71.